



Calibration of the Large Area X-Ray Proportional Counter (LAXPC) Instrument on board *AstroSat*

H. M. Antia¹, J. S. Yadav¹, P. C. Agrawal², Jai Verdhana Chauhan¹, R. K. Manchanda³, Varsha Chitnis¹, Biswajit Paul⁴,
Dhiraj Dedhia¹, Parag Shah¹, V. M. Gujar¹, Tilak Katoch¹, V. N. Kurhade¹, Pankaj Madhwani¹, T. K. Manojkumar¹, V. A. Nikam¹,
A. S. Pandya¹, J. V. Parmar¹, D. M. Pawar¹, Mayukh Pahari⁵, Ranjeev Misra⁵, K. H. Navalgund⁶, R. Pandiyan⁶, K. S. Sharma⁶, and
K. Subbarao⁶

¹ Tata Institute of Fundamental Research, Homi Bhabha Road, Mumbai 400005, India

² UM-DAE Centre of Excellence for Basic Sciences, University of Mumbai, Kalina, Mumbai 400098, India

³ University of Mumbai, Kalina, Mumbai 400098, India

⁴ Department of Astronomy & Astrophysics, Raman Research Institute, Bengaluru 560080, India

⁵ Inter-University Centre for Astronomy and Astrophysics, Pune 411007, India

⁶ ISRO Satellite Centre, HAL Airport Road, Bengaluru 560017, India

Received 2017 February 19; revised 2017 June 14; accepted 2017 June 15; published 2017 July 20

Abstract

We present the calibration and background model for the Large Area X-ray Proportional Counter (LAXPC) detectors on board *AstroSat*. The LAXPC instrument has three nominally identical detectors to achieve a large collecting area. These detectors are independent of each other, and in the event analysis mode they record the arrival time and energy of each photon that is detected. The detectors have a time resolution of 10 μ s and a dead-time of about 42 μ s. This makes LAXPC ideal for timing studies. The energy resolution and peak channel-to-energy mapping were obtained from calibration on the ground using radioactive sources coupled with GEANT4 simulations of the detectors. The response matrix was further refined from observations of the Crab after launch. At around 20 keV the energy resolution of the detectors is 10%–15%, while the combined effective area of the three detectors is about 6000 cm².

Key words: instrumentation: detectors – space vehicles: instruments

1. Introduction

The Large Area X-ray Proportional Counter (LAXPC) instrument on board the Indian Astronomy mission *AstroSat* consists of three co-aligned large-area proportional counter units for X-ray timing and spectral studies over the energy range 3–80 keV (Agrawal 2006; Yadav et al. 2016a). *AstroSat* was launched on 2015 September 28 with five major astronomy payloads (Agrawal 2006; Singh et al. 2014). Apart from LAXPC, these are the Ultra Violet Imaging Telescope, Soft X-ray Telescope, Cadmium–Zinc–Telluride Imager and Scanning Sky Monitor. The first four instruments are co-aligned so as to point to the same source. The LAXPC instrument is described in detail by Agrawal et al. (2017). The LAXPC detectors have a collimator with a field of view of about 1° × 1°. Each LAXPC detector is independent and can operate in event analysis mode, where the time of arrival of each photon is recorded to a time resolution of 10 μ s, giving an unprecedented sensitivity to a wide variety of timing phenomena. The detectors are filled with a xenon–methane mixture at twice atmospheric pressure and the detection volume has a depth of 15 cm, which gives large sensitivity at energies up to 80 keV.

This paper presents details of calibration for the LAXPC detectors. The preliminary calibration for the energy scale and energy resolution was carried out in a thermovac chamber on the ground using radioactive sources. These observations were compared with a GEANT4 (Agostinelli et al. 2003) simulation of the detectors to obtain the preliminary response matrix, as well as the background and field of view. These calibrations were refined by observations of the Crab and other known astronomical calibrators after launch.

The rest of the paper is organized as follows. Section 2 gives an overview of the instrument. Section 3 describes the ground calibration for energy resolution and energy scale. Section 4 describes the GEANT4 simulations and resulting response matrix. Section 5 describes in-orbit calibration using the Crab and Cas A sources. Section 6 describes attempts to characterize the background. Section 7 describes the long-term performance of the LAXPC detectors in orbit. Section 8 gives a summary of the calibration.

2. The LAXPC Detectors

The LAXPC instrument consists of three nominally identical proportional counters each with a geometric collection area of 100 × 36 cm². The detectors are labeled as LAXPC10, LAXPC20, LAXPC30 (LX10, LX20, LX30 in brief). Figure 1 shows a schematic diagram of the LAXPC detector including the collimators and shield. Each detector has five anode layers, each consisting of 12 anode cells of size 100 × 3 × 3 cm³. The top two layers are divided into two parts with alternate cells connected. These gives seven main anodes—A1 and A2 in the top layer, A3 and A4 in the second layer from the top, and A5, A6, and A7 in the remaining three layers. The main anodes are surrounded on three sides by veto cells of thickness 1.5 cm. The veto anode A9 covers the bottom area (100 × 39 cm²), while veto anodes A8 and A10 cover the two sides (100 × 15 cm²). The configuration of anodes is shown in Figure 2. The two sides (36 × 15 cm²) perpendicular to the length of the cells do not have any veto anode. The cells are labeled C1, C2, ..., C11, C12 from right to left in the figure. Thus cell C1 is adjacent to veto anode A8, while cell C12 is adjacent to veto anode A10.

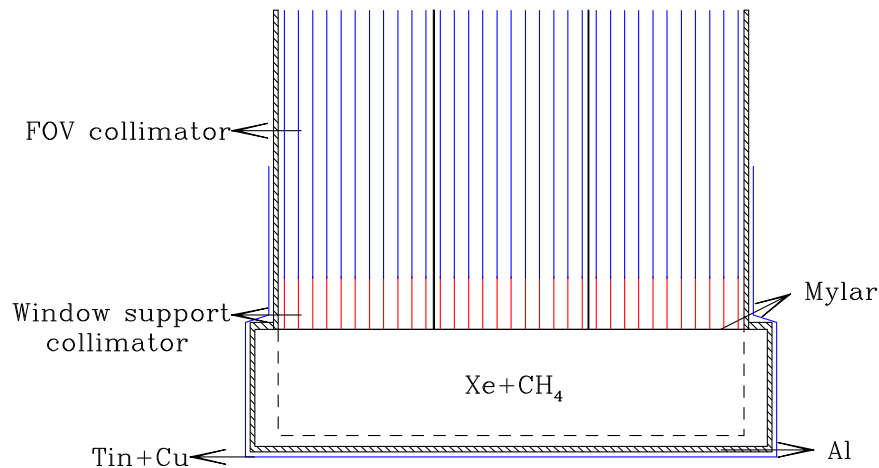


Figure 1. Schematic diagram showing the LAXPC detector. The dashed lines in the chamber mark the active volume of the detector covering the main anodes.

The entire volume of detectors LAXPC10 and LAXPC20 is filled with a mixture of xenon (90%) and methane (10%) at a pressure of about 2 atm. LAXPC30 has a mixture of xenon (84.4%), methane (9.4%), and argon (6.2%) at a pressure of about 2 atm. The reason for using a different gas mixture in LAXPC30 was that after filling the first two detectors it was noticed that the energy resolution at 60 keV was about 13% with the high voltage employed to get the required energy range. Hence it was decided to add a small amount of argon in LAXPC30 because that is expected to improve the energy resolution (Rao et al. 1987). The low-energy threshold is kept at about 3 keV. The top of the detector is sealed by a 50 μm thick aluminized Mylar window, which allows X-rays with energy >3 keV to pass through and dictates the low-energy threshold of the detectors. Only events with a larger energy can trigger the electronics. The Mylar window covers only the active detector volume. The veto anodes on the two sides are covered by an aluminum box and shield and are not expected to receive incident photons coming from the top.

The LAXPC detectors are similar to the Proportional Counter Array on the *Rossi X-ray Timing Explorer (RXTE-PCA)*, which was launched in 1995 (Jahoda et al. 2006). The main differences are the increased pressure and depth of the detector, which gives a high effective area at higher energies (>30 keV). At the same time a larger detector volume increases the background in LAXPC, thus making it difficult to study faint sources. A higher pressure in LAXPC also degrades the energy resolution to some extent. Another major difference is the availability of event mode data, which give the arrival time and energy of each photon that is detected. This allows detailed timing studies for all sources that are observed. Apart from these, there are differences in the nature and distribution of veto layers, which may also contribute to differences in the background.

An analog-to-digital convertor (ADC) converts the signal to 10 bit digital form, giving 1024 energy channels. Considering an energy resolution of about 10%, the number of channels can be reduced to 512 or 256 by combining two or four consecutive channels. This appears to be desirable because the output shows some fluctuations between even and odd channels. These fluctuations are of a few percent in magnitude, and the ratio of counts in consecutive channels is independent of time. This can be seen in residuals after fitting the spectrum. For LAXPC10 and LAXPC30, 512 channels are adequate, while

for LAXPC20 we need to go down to 256 channels. This truncated range is implemented in the *LaxpcSoft* software, while other level-2 pipeline software⁷ produces 1024 channel output for all detectors.

The Mylar window is supported against the gas pressure by a collimator of height 7.5 cm made of square aluminum cells, termed the window support collimator. The field-of-view collimator of height 37 cm is placed above the window support collimator. Both these collimators have aligned gaps with a pitch of 7.0 mm. The field-of-view collimator has a tin sheet sandwiched between copper and aluminum using epoxy. This gives a field of view of about 0.9×0.9 . Since aluminum in the window support collimator is almost transparent to higher energy X-rays, the field of view increases at high energies because only the field-of-view collimator of length 37 cm is effective. The detector is covered by a tin shield of thickness 1 mm, coated with copper (50 μm) on five sides. On the sides of the detector the cover extends from the bottom to 23 cm above the top of the detector, thus covering the lower part of the collimator housing. This shield is effective in cutting off the background from low-energy photons and charged particles.

The outputs from the seven main anodes and three veto anodes are fed to 10 charge-sensitive preamplifiers (CSPAs). The high voltage is supplied to all main anodes (A1–A7) at the same point and its value is therefore the same. The veto anodes have a lower voltage but it cannot be controlled separately. The overall high voltage can be adjusted from ground in appropriate steps. But the high voltage of an individual anode cannot be adjusted. Hence, gain equalization is achieved by varying the gain of the corresponding CSPA of the anode. Gain equalization is done on the ground by matching the 30 keV Xe K-escape peak in background or an ^{241}Am source for each individual anode. The CSPA gain cannot be adjusted after launch. The high voltage is switched off when the satellite is passing through the region of the South Atlantic Anomaly (SAA).

If more than one anode is triggered within the time resolution, the signal is simultaneously recorded in all these anodes. In order to reject background events the processing electronics is designed to reject any event that satisfies the following criteria:

1. Any event that triggers any of the veto anodes (A8–A10).
2. Any event that deposits more than the upper limit of about 80 keV in any anode.

⁷ http://www.tifr.res.in/~astrosat_laxpc/software.html

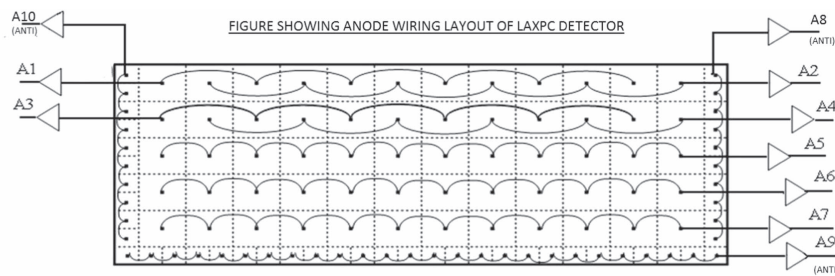


Figure 2. Configuration of anodes in the LAXPC detectors. The figure shows a projection on a plane perpendicular to the length of the anode cells ($39 \times 16.5 \text{ cm}^2$). The cells in the main anodes are labeled C1 to C12 from right to left in the figure.

3. Any event that is recorded in more than two main anodes (A1–A7).
4. Any event that is recorded in two main anodes (A1–A7) and the energy in both anodes is not in the range of xenon K X-rays covering about 25–35 keV. In this case if energy in any one or both anodes is in the K X-ray range then the event is accepted, energies in the two anodes are added, and the event is recorded as a single event of the combined energy.

This logic is found to be effective in reducing the background by about 99% (Section 4.4).

Thus the events that are accepted are either single events where only one main anode is triggered or double events where two main anodes are triggered but the energy in at least one of them is in the Xe K X-ray range. In both these cases, the energy deposited in these anodes should be below the upper energy threshold. Since the threshold is applied to each anode separately, the double events can exceed the energy threshold by up to about 35 keV. Further, since the detector response is not linear, the double events may not be recorded at the same channel as a single event with the same total energy. The lower and upper thresholds for the Xe K X-ray range can be set remotely for each detector, but they apply to all anodes in a detector.

The energy resolution of the detector can degrade with time if impurities accumulate in the gas. On the ground this could happen by diffusion through the Mylar window, but in the vacuum of space the rate of accumulation of impurities would be small. To take care of impurities, a gas purification system is included in the detector, which may be used from time to time to maintain the energy resolution close to the optimum value.

A system timebase generator (STBG) provides a stable and accurate time reference for each of the three LAXPC detectors. The time reference has a resolution of $10 \mu\text{s}$ but has a slow drift. The STBG time is correlated to UTC time from an onboard SPS time to correct for the drift, which is of the order of 1 part in 10^5 or about 1 s in a day. Extensive tests were carried out on the ground and the corrected time is found to be satisfactory to the required accuracy even if SPS time is not available for an hour. In practice, SPS time is almost continuously available, thus giving the required timing stability. The STBG also provides a time reference for other science payloads on *AstroSat*.

The LAXPC detectors have two main modes of operation—event analysis (EA) mode and fast counter (FC) mode. In the event analysis mode, which is the default, the timing of each event is recorded along with information about the anode ID where it is recorded as well as the energy (channel number).

Each event gives rise to five bytes of data. In this mode the dead-time of the detector is estimated to be about $42 \mu\text{s}$ (Yadav et al. 2016b). The LAXPC processing electronics is a non-paralysable system, so an event occurring during the dead-time following the previous event is simply lost. Thus with an increasing event rate it will reach a saturation rate equal to the inverse of the dead-time. The dead-time was measured on the ground using an X-ray gun to give a high count rate. The measured count rate from the processing electronics was compared with that obtained from a commercial multichannel analyser (MCA8000A), which gives the dead-time-corrected count rate. The dead-time can also be measured by taking a Fourier transform of time series for a bright source, which would give a broad peak close to the inverse of the dead-time in the power spectrum. This can be compared with that expected for a dead-time-corrected Poisson level power (Zhang et al. 1995). This yields an estimate of dead-time of around $42 \mu\text{s}$ (Yadav et al. 2016b). It is also possible to estimate the dead-time by comparing the observed count rate and the count rate estimated from the slope of a δt plot, which shows the distribution of time intervals between two consecutive events, which should show an exponential behavior for events with a Poisson distribution. This technique also gives a value of about $42 \mu\text{s}$. There is also a smaller dead-time of about $35 \mu\text{s}$ associated with rejected events, e.g., those that exceed the upper level discriminator (ULD) threshold, or those that trigger the veto anode, or those that trigger more than two anodes simultaneously.

Operation in event mode also generates broadband counting (BBC) mode data simultaneously. These data contain counts in a predefined time bin in four different energy bins in three layers, as well as some other counts for diagnostic purposes. The four energy bins are 3–6 keV, 6–18 keV, 18–40 keV, and 40–80 keV. Layer 1 combines anodes A1 and A2, layer 2 combines anodes A3 and A4, while layer 3 combines A5, A6, and A7. The time bin can be set from 16 ms to 2048 ms in steps increasing by a factor of 2, with a default value of 128 ms. Since these counters are 10 or 11 bits deep, they may overflow for bright sources if a time bin of size toward the long end of the allowed range is selected. For example, for the Crab the counters may overflow if a time bin greater than 256 ms is used. It may be noted that in all cases the event mode data are always available to get the correct light curve in any energy and time bin. Apart from genuine events, the BBC mode also has counters for rejected events, e.g., those exceeding the ULD in the main anodes (A1–A7) or those that trigger veto anodes.

In the FC mode the counts in only the top layer in a fixed time bin of $160 \mu\text{s}$ are recorded in four energy bins. In this mode the rejection of events using veto anodes and mutual

coincidence is suppressed and all events registered in anode A1 or A2 are counted. The approximate energy bins are 3–6 keV, 6–8 keV, 8–12 keV, and 12–20 keV. These counters are 8 bits deep. This mode may be useful for bright or flaring sources where the count rate is very high. In this case the dead-time of the detector is about 10 μ s and hence much higher count rates can be recorded.

Apart from these, there is also the anti-bypass mode where the rejection of events through veto anodes is suppressed. This is used for onboard calibration using a radioactive ^{241}Am source, which is placed in the veto anode A8. This is used to check the energy resolution and shift in gain. Even in default mode a fraction (1/128) of events in veto anodes are recorded and can be used for checking the energy resolution and gain if sufficiently long observation is available. If the resolution degrades then we can perform purification of the detector gas, while the shift in gain can be compensated by a change in high voltage. It is important to keep the gain close to the ground setting to ensure that double events are handled correctly. The energy spectrum of a background or faint source also shows a peak around 30 keV due to Xe K fluorescence X-rays, which can also be used to monitor the shift in gain.

3. Calibration on the Ground

To obtain the energy resolution and gain of detectors, three radioactive sources at different energies in the range of the LAXPC detectors were used. The calibration was performed in a thermovac chamber and measurements were repeated at three temperatures of 10°C, 20°C, and 30°C to study the temperature dependence of the detector response. The following three sources were used:

1. ^{55}Fe with energy of 5.9 keV. These X-rays are absorbed in the top layer and hence only the two top anodes A1 and A2 register these events. Hence, the anodes A3–A7 are only calibrated using energy beyond 20 keV.
2. ^{109}Cd with energies of 22.1 keV (54.5%), 21.9 keV (28.8%), 24.9 keV (13.7%), and 88 keV (3.0%). The first two peaks cannot be resolved by the detector, while the third one gives a small feature at the high end of the main peak, which can be fitted with some effort. The last peak is beyond the range of the detector, though because of finite resolution one should, in principle, detect a small, low-energy tail of the peak, as well as the contribution from double events, or when the Xe K fluorescence X-ray escapes the detector. However, the resulting peak is too weak and was not detected. At 22 keV about 50% of photons are absorbed in the top layer, but there are significant counts in all layers. The ratio of counts in different layers is determined by the gas density, and we could use this to estimate the density in each detector, which is required to generate the detector response.
3. ^{241}Am with energy of 59.6 keV. This source also gives multiple peaks because of the loss of energy due to Xe K fluorescence X-rays escaping the detector. The detector logic is built to add contributions in two anodes if at least one of them is in the range of Xe K fluorescence X-rays (25–35 keV). Hence, we get additional peaks at 29.8 keV (due to escape of Xe K_{α}) and 25.2–26.0 keV (due to escape of Xe K_{β}). The Xe K_{α} X-rays account for about 81% of Xe K X-rays, thus giving a dominant peak at 29.8 keV. The second peak due to K_{β} X-rays is barely

resolvable with the detector resolution. Apart from these, the 59.6 keV peak is also split into two parts, one coming from single events where all energy is deposited in a single anode, and the other from double events where the energy is split between two anodes and the contribution is added by the detector logic. Since the detector gain is not strictly linear but has a small quadratic term, the channel number of a double event does not coincide with that for a single event, but the two peaks cannot be resolved properly, though they can be fitted with some effort. The contribution of single and double events can be separated by analyzing these events separately. Since the quadratic term is negative the single-event peak occurs at a lower channel than that from double events. The energy resolutions of the two peaks are also different. The energy resolution of the double peak is determined by the energy resolution at 29.8 keV because the dominant component is from two 29.8 keV components. Thus the absolute energy resolution of a 59.6 keV double-event peak is $\sqrt{2}$ times that for 29.8 keV, and the relative energy resolution is $1/\sqrt{2}$ times that for 29.8 keV. On the other hand, the resolution of the peak due to single events is much worse than that for double events. By fitting these two peaks around 59.6 keV, it is possible to estimate the quadratic term in the mapping from energy to channel number.

To estimate the detector background, the counts are recorded without any source, before and after the source measurements are made. The background count rate is then subtracted from that for the source to get the contribution from the source.

In order to perform the calibration inside the thermovac chamber, an x - y motion platform was designed for movement of radioactive sources above the field-of-view collimator. This can hold all three sources and expose one or more of them at a time. The x - y motion platform can function in vacuum and its movements and source on/off status can be remotely controlled. The movement of sources is controlled by a program that moves the source with a predetermined pattern in the x or y direction. The pattern was chosen to cover the entire area of the detector over about 2 hr. To study the behavior of each cell, in some cases the source was moved along the length of each of the 12 cells.

To check the long-term stability of detectors, periodic measurements were made on the ground over a period of several months to check for drift in the position of the peak channel. A slow decrease in the peak channel with time was found due to accumulation of impurities in the gas. The original position was restored when the gas was purified. Similar monitoring is continuing after launch. All detectors were filled with gas by 2011 and no leak was noticed before launch. This will put a limit of less than 0.5% per year on the leak rate before launch for all three detectors.

Apart from energy resolution, the timing characteristics of the detectors were also tested on the ground. A Fourier transform of the time series did not show any peak at frequencies less than 2 kHz. When a strong source from an X-ray gun was used the Fourier transform showed a peak around 15 kHz, which is expected from the dead-time effect. This is confirmed by the observations in orbit (Yadav et al. 2016b). The distribution of the time interval between two consecutive events in the LAXPC detectors follows the expected exponential behavior for a Poisson distribution. It

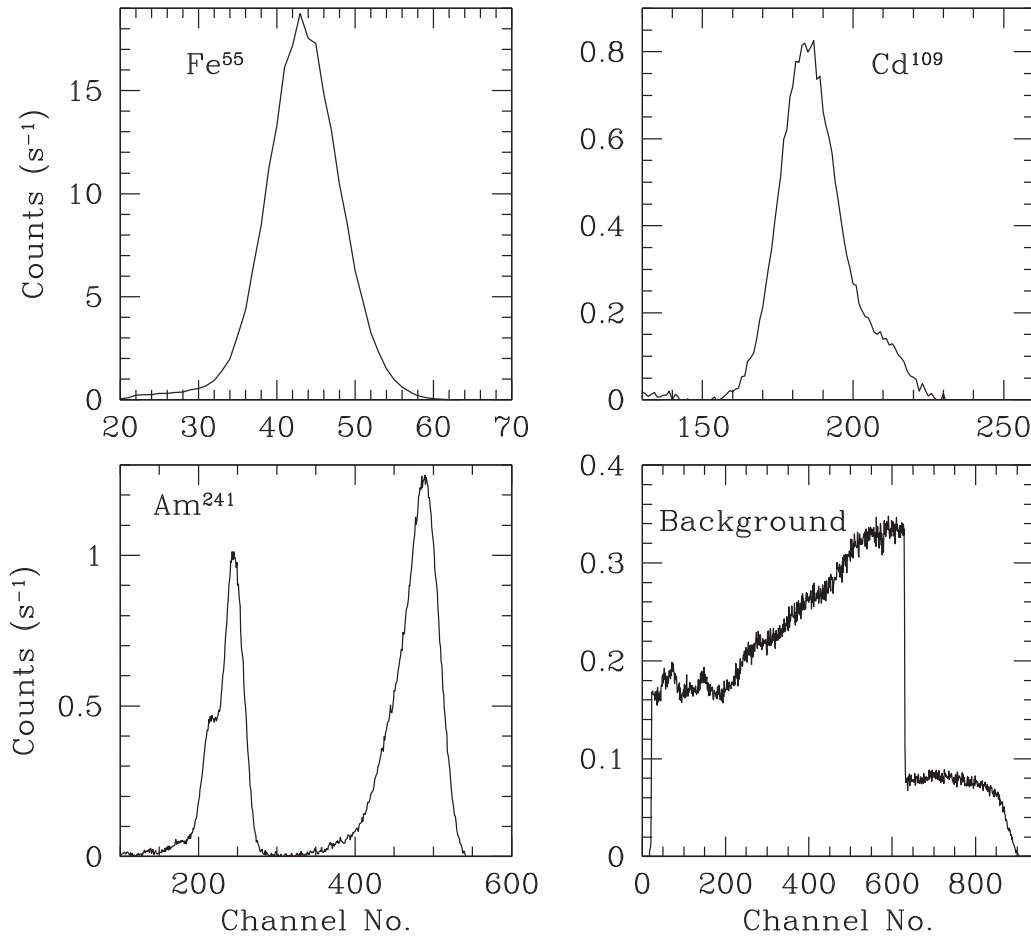


Figure 3. The spectra for the three radioactive sources after correcting for the background and the background spectrum for LAXPC30 as observed on the ground.

also shows a cutoff at $50 \mu\text{s}$, in agreement with the measured dead-time.

The operation in fast counter (FC) mode was also tested on the ground using radioactive sources as well as the X-ray gun, and again no peaks were found in the Fourier transform up to the Nyquist frequency of 3125 Hz. The nominal boundary of different energy bins was also tested by comparing the data in FC mode with the spectrum in EA mode for the same source. The boundaries of the energy bins were found to be correct to within about 1 keV.

3.1. Energy Resolution of LAXPC

The energy resolution R of the LAXPC detector, averaged over the entire area, was measured for each of the X-ray lines from the radioactive sources. The energy resolution is defined by

$$R = \frac{\text{FWHM}(\text{channels})}{\text{Peak}(\text{channels})} \times 100\%. \quad (1)$$

To estimate the resolution, the observed spectrum for the source is corrected for the background and then fitted to a sum of Gaussian profiles to obtain the peak position and resolution. The observed spectra for the three sources and the background obtained by adding the counts in all anodes (A1–A7) are shown in Figure 3. These spectra were fitted to obtain the peak position and resolution and the results are shown in Figure 4 for three different temperatures and for different detectors at 20°C .

The background spectrum in Figure 3 shows the lower and upper energy thresholds beyond which the count rate drops sharply. On the lower side, it drops to zero below the lower energy threshold as the anodes are not triggered. Beyond the ULD the count rate does not drop to zero because the contribution from double events is still accepted. This is because this threshold is applied separately to each anode and the sum of the energies in two anodes can exceed the threshold. Thus, in principle, LAXPC can detect photons with energies up to about 110 keV, though the efficiency reduces beyond 80 keV as only the double events contribute. From the magnitude of the drop around channel 640, it appears that double events account for 25%–30% of all events at these energies in the background spectrum.

It can be seen from Figure 4 that the resolution improves as temperature increases, while the peak channel shifts to a lower value. In orbit, the temperature of the detectors is maintained through heaters, and its variation by less than 2°C may not be significant. This resolution is calculated when the counts in all anodes are added. If we consider a single anode or a single cell in an anode the resolution is better by 1%–2%. This is because the gains of all anodes may not be perfectly aligned and the scatter between different anodes broadens the peak slightly. Similarly, the two end cells in each layer (C1 and C12) have a different gain than the middle cells. The difference is about 5% and has to be accounted for while constructing the response matrix. This variation also adds to the width of peaks. Below

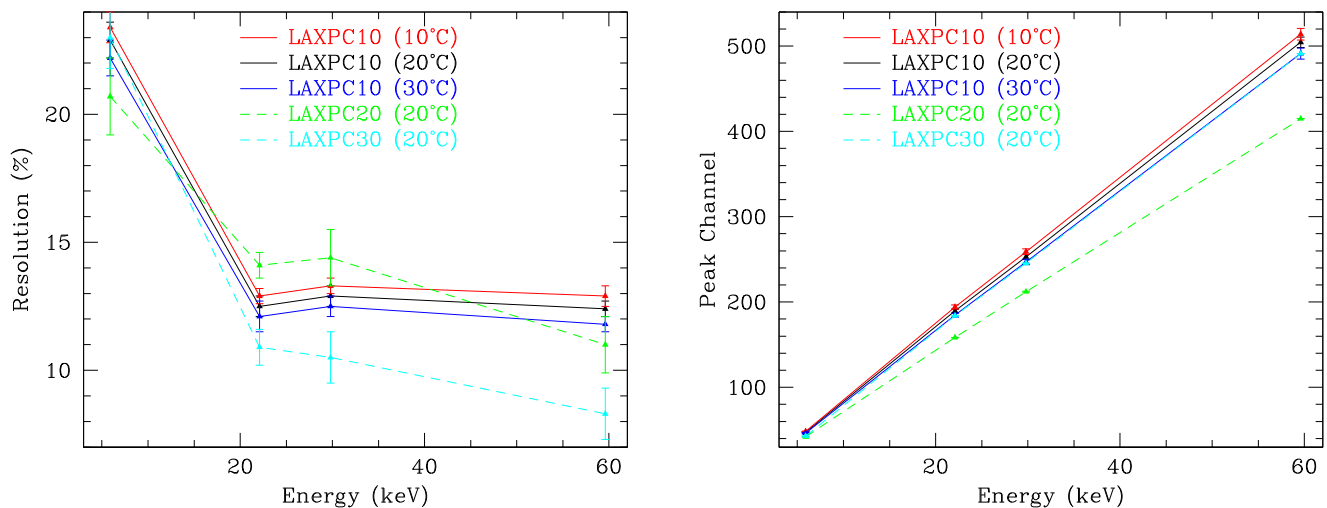


Figure 4. The energy resolution (left panel) and peak position (right panel) for LAXPC detectors as determined from observations on the ground using radioactive sources.

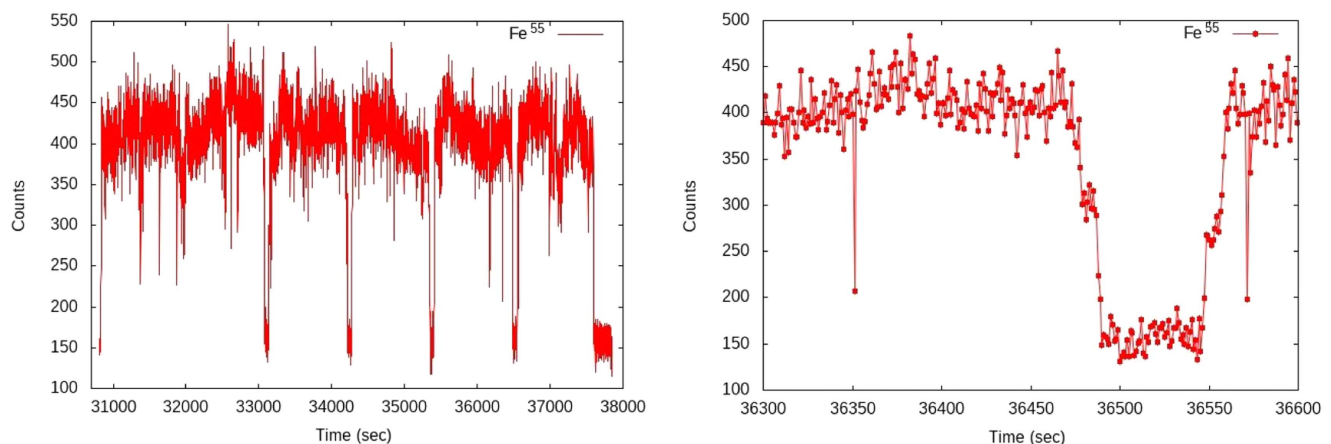


Figure 5. Count rate during a scan across the LAXPC20 detector using the ^{55}Fe source. The right panel shows part of the scan after magnification. The big dips are due to the source moving outside the detector area during the scan.

20 keV the energy resolution varies as $1/\sqrt{E}$ as expected for a proportional counter (Knoll 2000).

From Figure 4(b), it appears that the relation between energy and channel number is almost linear. This is misleading because the peak around 59.6 keV is actually a combination of two peaks that are not resolved in the fit. Similarly, the energy resolution appears to remain flat at high energies, which is also misleading due to the compound nature of the 59.6 keV peak. It can be seen that the gains of LAXPC10 and LAXPC30 are similar, but that for LAXPC20 is lower. Further, the gain in cell C1 of anode A4 in LAXPC10 is about 75% of that for the other cells, and this gives rise to a small second peak on the lower energy side (see Figure 7). This difference has to be accounted for while generating the response matrix.

The veto anode A10 in LAXPC10 failed during the thermovac test and has been disconnected. As a result, the background is higher in this detector than in the other two. Since launch, the gain of LAXPC30 has been shifting steadily due to a suspected minor leak. As a result, the high voltage of this detector is periodically adjusted to keep the gain close to the ground value.

The count rate was not uniform over the entire area of the detector and variations of a few percent were observed,

presumably because of nonuniformity in the collimator. Figure 5 shows the scan over LAXPC10 detector using the ^{55}Fe source. The prominent dips at regular intervals are due to the source moving outside the detector area during the scan. But there are other smaller dips that are likely to be due to blockages in some collimator cells. The blocked area was found to be less than 1% of the scanned area. There were also some fluctuations in the count rate over a timescale of minutes. These variations are most likely due to nonuniformity in the collimator. Apart from these, there are fluctuations over a timescale of 10 s, due to the source crossing the collimator cell boundary. These show up clearly in the Fourier transform. Since the radioactive sources are kept just above the collimator, they are expected to illuminate only one or two collimator cells at a time. If the source is moving almost exactly above the boundary of a cell, it can illuminate up to four cells simultaneously. As it moves from one cell to the next, part of the beam will be blocked by the boundary of the cell, thus causing a dip in the counts. From these scans it is difficult to estimate the transmission efficiency of the collimator. This was later estimated in orbit using a scan over the standard Crab X-ray source.

4. GEANT4 Simulation

In order to understand the characteristics of the LAXPC detectors and to construct the response matrix, GEANT4 (Agostinelli et al. 2003) simulations were carried out. For this purpose the basic detector geometry, including the aluminum box, shield, Mylar window, and collimators, was included to define the detector. Other features such as electronics, purification system, and the anode and cathode wires inside the detector were omitted for simplicity. The advantage of using GEANT4 simulation is that all physical processes describing the interaction of charged particles and photons are included and absorption coefficients of all relevant materials are incorporated. Similarly, all particles including secondaries, such as photons, electrons, protons, muons, etc., are tracked. Further, the loss of efficiency due to escape of Xe K and L X-rays is automatically included in the simulations once the anode boundaries are specified. We did not include any dead zone between two anodes where the interaction may not be recorded. The GEANT4 package can deal with particles in the energy range 100 eV–100 TeV. All secondary particles in this energy range are followed until they interact or move outside the defined volume. Apart from the response matrix and efficiency of the detector, the simulations were also used to estimate the field of view of the collimator as well as to estimate the background from photons and charged particles.

The simulations typically use 10^6 – 10^7 photons, which in most cases were incident perpendicular to the Mylar window at the top. Further, these particles are uniformly distributed over the active detector area. These simulations were tested by comparing the results with observations from radioactive sources described in Section 3.1. To estimate the field of view of the collimator, the photons were assumed to be arriving at a small angle to the axis of the detector. To estimate the background, the particles were assumed to be arriving isotropically from all directions and to be uniformly distributed on all bounding surfaces.

4.1. The Detector Response and Efficiency

In order to approximate the observations of radioactive sources, simulations were carried out with the same distribution of energy as expected from these sources. The simulations yield the energy deposited in each anode cell from any event. The same logic as used in the detector electronics was applied to reject or accept the event. The result was compared with the observed spectrum. Since the absolute strengths of the sources were not known because they were collimated through a small hole in the container and placed over the field-of-view collimator, the number of events accepted by the simulation in a broad energy band covering the peak was normalized to match the number of counts observed in the same range. Thus the normalization was not a free parameter in the simulation. Once the normalization of the simulated spectrum was fixed, the counts in each anode and channel were compared with the observed spectrum.

The voltage pulse in a proportional counter is only approximately proportional to the energy deposited in a given anode; instead, the pulse is proportional to the number of electrons produced in the corresponding anode. The observed pulse height is essentially the number of electrons produced in the gas multiplied by the electronic gain from the proportional counter and the amplifier. To generate the response matrix we

need a mapping from the energy deposited to the pulse height channel that is recorded. For this purpose, following Jahoda et al. (2006), we define an energy scale, E_p , proportional to the number of electrons produced, but normalized such that it is approximately equal to the energy deposited, E . The average energy $w(E)$ required to produce one ionization electron in Xe is close to 22 eV (Dias et al. 1991, 1993, 1997). It is convenient to define

$$E_p = \frac{22.0 \text{ eV}}{w(E)} E. \quad (2)$$

The function $w(E)$ is shown in Figure 4 of Jahoda et al. (2006) and has discontinuities at the xenon K- and L-edges. As a result of this, the energy-to-channel mapping may not be monotonic in this region. This function is used in the simulation to calculate E_p , which is then used to calculate the corresponding channel.

In order to calculate the spectrum of simulated events we need a mapping from energy to channel. This was provided by the observed positions of the peaks in spectra for radioactive sources. We used a quadratic function

$$n_c = e_0 + e_1 E_p (1 + e_2 E_p), \quad (3)$$

to fix the energy-to-channel mapping. Here, E_p is the effective energy in keV as defined above, and n_c is the ADC channel where energy is mapped. The parameters e_0 and e_1 are determined by matching the 5.9 keV peak in the ^{55}Fe spectrum, the 22.1 keV peak in the ^{109}Cd spectrum, and the 29.8 keV peak in the ^{241}Am spectrum. The parameter e_2 was determined by fitting the 59.6 keV peak in the ^{241}Am spectrum. One more iteration was performed by recalculating e_0 and e_1 with fitted value of e_2 . Since the position of low-energy peaks is not sensitive to e_2 one iteration was found to be sufficient.

Near the absorption edges of Xe the mapping given by Equation (3) is further tuned to fit the observed spectrum of the Crab. Since the temperature in orbit is maintained constant to within 2°C, no temperature dependence of coefficients in Equation (3) is required. The same is true for energy resolution also.

The relative number of counts (total counts under a peak) in different anode layers depends on the absorption coefficient and density (or pressure) of the gas. Using this ratio for the ^{109}Cd source, which shows a systematic variation in counts with layers, it is possible to estimate the density of the gas. It was found that varying the density by a few percent can get the relative count rates into better agreement. To estimate the density of the gas, simulations were done with different values of density and the relative difference in count rates

$$F(\rho) = \sum_{i=1}^5 \left(\frac{O_i - S_i}{O_i} \right)^2, \quad (4)$$

where O_i and S_i are respectively, the counts in the observed and simulated spectra in the i th layer. The sum is over the five layers. Since the total counts in the observed spectrum are of the order of 10^6 , the statistical errors in O_i are very small and any departure in $F(\rho)$ from zero is due to systematic discrepancies in the simulation. As a result, we have not tried to define a χ^2 function for this purpose. This function shows a well-defined minimum as a function of density as shown in Figure 6. The difference in density could arise due to a small

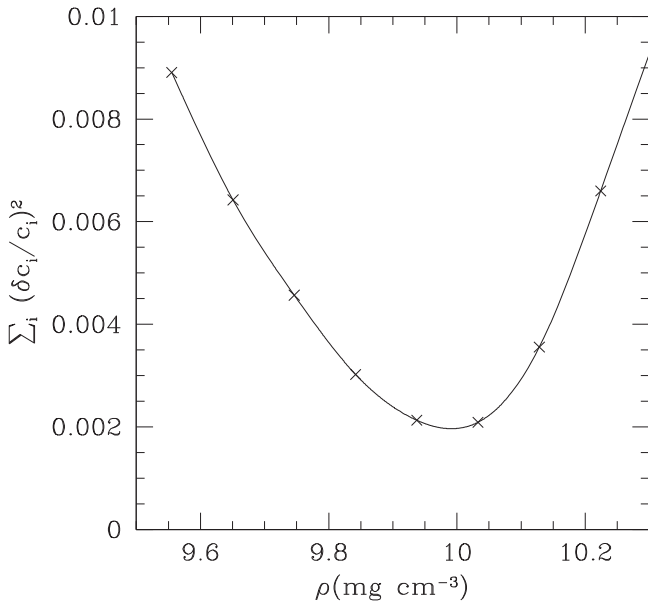


Figure 6. The function $F(\rho)$ as defined in Equation (4) is shown for LAXPC10.

variation in pressure or temperature. This value of density is used in all further simulations. The density is found to be 10.0 mg cm^{-3} in LAXPC10, 10.7 mg cm^{-3} in LAXPC20, and 11.5 mg cm^{-3} in LAXPC30.

Apart from the energy-to-channel mapping we also need the energy resolution as a function of energy to calculate the detector response. In principle, we can use the measured resolution shown in Figure 4 for this purpose, but that is not satisfactory because it will not leave any free parameter in the simulations to match the observed spectrum for the radioactive sources. Further, the peak at 59.6 keV in the ^{241}Am spectrum is a multiple peak arising from single and double events with different resolutions and channels. Thus we keep the energy resolution as a free parameter in simulations, and it is determined by matching the observed spectrum. Thus we have four free parameters that give the energy resolution for the four peaks at 5.9 , 22.0 , 29.8 , and 59.6 keV . The 5.9 keV peak is not seen in lower layers and its resolution is determined by the top layer only. In any case, here we have assumed that all anodes have the same resolution. The 22.0 keV peak in ^{109}Cd has a small component around 25 keV , but we assume the same relative resolution for the entire peak. Similarly, the 29.8 keV peak in the ^{241}Am spectrum also has a contribution at lower energy from the escape of Xe K_β X-rays, but we assume the same relative resolution for the entire peak. The 59.6 keV resolution applies to the peak from single events where all energy is absorbed in the same anode. For the double events the two events have energy close to 29.8 keV and that resolution is used in each anode, before the channel numbers in the two anodes are added to get the final value. Thus we have only eight free parameters— σ_1 , σ_2 , σ_3 , σ_4 to specify the energy resolution, e_0 , e_1 , e_2 (Equation (3)), and the density—to match the three spectra in each anode. Only the regions near the peaks are used to fit the spectra.

To determine these parameters we first determine e_0 , e_1 by matching the peak positions and then σ_2 and density are determined to match the ^{109}Cd spectrum for all anodes. This fixes the value of density as explained above, and this is used in

all further simulations. Then the ^{55}Fe spectrum is fitted to obtain the resolution σ_1 . Since the low-energy photons are absorbed in the top layer we only need to fit the spectrum in anodes A1 and A2. The other three parameters, σ_3 , σ_4 , e_2 , are used to match the spectrum for ^{241}Am . The resulting fits are shown in Figure 7 for LAXPC10. The anode A4 shows a secondary peak on the lower side, due to the difference in gain in cell C1.

The resolutions obtained by fitting the simulated spectrum for the 5.9 , 22.1 , 29.8 keV lines are close to those determined by fitting the observed spectrum described in Section 3.1. However, for the 59.6 keV peak the resolution obtained by fitting the simulated spectrum is much poorer than that from fitting the observed spectrum directly. This is because the simulated spectra give the resolution for the peak defined by single events, while the fit to observed spectra did not attempt to resolve the two peaks. It is possible to fit the two peaks but in that case the fit is not very stable. To illustrate the difference we show in Figure 8 the observed spectrum for ^{241}Am when only single or double events are included. It can be seen that the peak in single events is broader and shifted to a lower channel as compared to that in double events. The resolution obtained by fitting the simulated spectrum matches that for single events. The shift to the negative side occurs because the quadratic term in Equation (3) is negative. The values of the parameters defining the gain for the detectors are listed in Table 1.

The inclusion of double events in the detector logic does introduce some complication in the construction of the response matrix, but this is needed because typically 30% of the events above the K-edge of xenon are double events and their exclusion will reduce the efficiency significantly. The reduction in efficiency would be about 40% because in another 30% of the events the Xe K fluorescence X-ray escapes the detector and the event is recorded at lower energy. The event mode data from the detectors give the channel information for each anode, and it is possible to reject these double events in software, though the current pipeline software does not have that option. Figure 9 shows the observed spectrum of the Crab in LAXPC10 when the double events are excluded. It can be seen that at high energies the efficiency is reduced by about 40% when double events are excluded. Further, excluding a double event will not remove all complications in the response matrix, because at energies above the K-edge of xenon a significant fraction of single events also correspond to cases where the xenon K X-ray has escaped the detector, and this will have to be considered anyway while generating the response, because there is no way this event can be distinguished from an event produced by a lower energy photon.

The observations of radioactive sources give the resolution at only four energy values, while we need the energy resolution for all energies in the range of LAXPC to construct the response matrix. To obtain this we use a fit to σ^2 by a linear B-spline basis function using three knots in $1/E$. We fix the knots at $1/80$, $1/28$, $1/3 \text{ keV}^{-1}$. This gives a piecewise linear approximation in $1/E$. Figure 10 shows the energy resolution and energy-to-channel mapping as determined from simulations. This can be compared with Figure 4, which is based on fitting the observed peaks in spectra for radioactive sources. The main difference arises for energies above 35 keV and is due to the composite nature of the peak in this region. The larger nonlinearity in LAXPC20 is clearly seen in Figure 10.

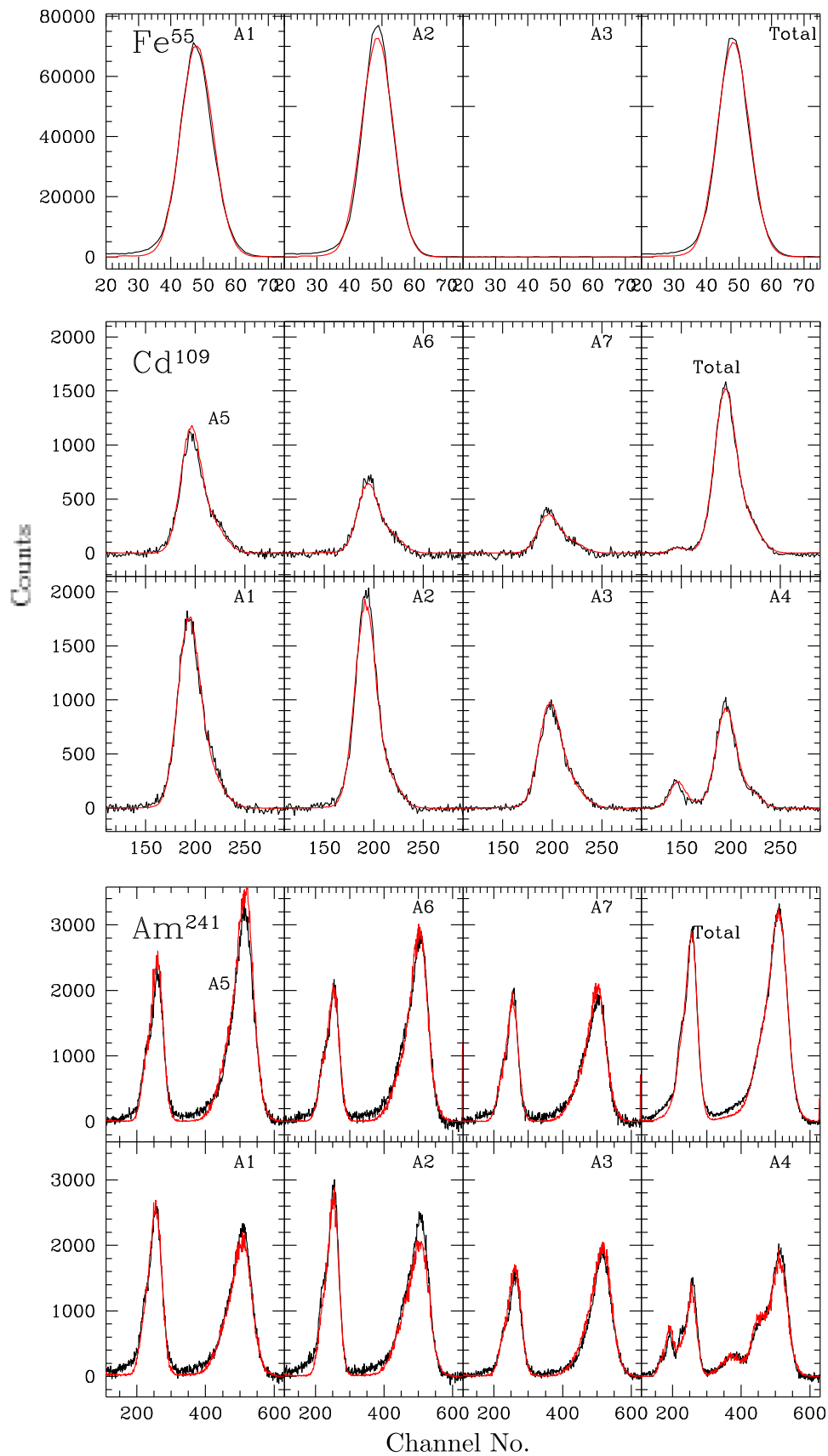


Figure 7. The fits to observed spectra for radioactive sources by simulations for LAXPC10. The black lines show the observed spectrum while red lines show the simulated spectrum. The counts in the panel for combined spectra are scaled down to fit on the same axis. The anode A4 shows a secondary peak on the lower side, due to the difference in gain in cell C1.

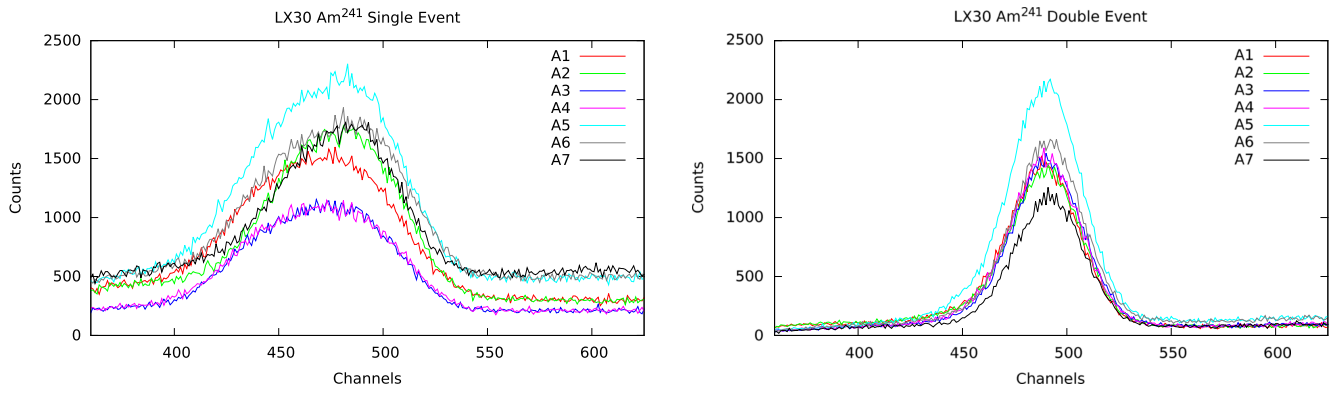


Figure 8. The observed spectrum of ^{241}Am in LAXPC30. The left panel shows the spectrum when only single events are included, while the right panel shows the spectrum when only double events are included.

Table 1

Parameters, e_0 , e_1 , and e_2 (Equation (3)) for the Three LAXPC Detectors

Detector	e_0	e_1	e_2
LAXPC10	-3.46 ± 0.05	8.936 ± 0.010	-0.00198 ± 0.00010
LAXPC20	$+0.08 \pm 0.10$	7.564 ± 0.015	-0.00267 ± 0.00010
LAXPC30	-7.67 ± 0.05	9.022 ± 0.015	-0.00197 ± 0.00010

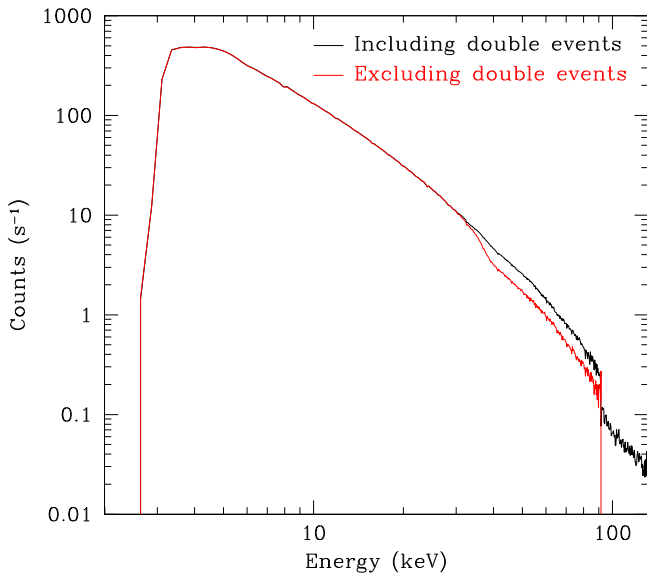


Figure 9. The background-subtracted spectrum of the Crab observed during 2017 January in LAXPC10 by including (black) and excluding (red) the double events.

Because of this nonlinearity the effective ULD is higher in LAXPC20.

Using the energy-to-channel mapping and the energy resolution shown in Figure 10, it is possible to simulate the detector response for any incident energy in the relevant range. From these simulations it is possible to calculate the response matrix, which provides information about the probability that an incident photon of any given energy will be observed in a particular channel of a particular anode. By summing over the probabilities in all channels and anodes we can get the detector efficiency at that energy, which is the probability that a photon of given energy will be observed in the detector. This efficiency multiplied by the geometric area of the detector would give the effective area of the detector.

4.2. The Effective Area of LAXPC Detectors

To calculate the effective area we carry out simulations with incident photons at various energies and calculate the fraction that would be detected by the detectors. The geometric area of each LAXPC detector is $100 \text{ cm} \times 36 \text{ cm} = 3600 \text{ cm}^2$. Assuming a perfectly aligned collimator in the simulations, we find that at best 79% of photons are detected because the rest of the area is blocked by the collimator. This gives an area of about 2800 cm^2 for each detector. This would give a total effective area of three detectors around 8400 cm^2 . From the calibration on the ground it was impossible to estimate the effect of imperfections in the collimator. In particular, even the alignment of the collimator may not accurately match that of the aluminum box containing the collimator, which was used to align the detectors on the satellite deck. Since all instruments on *AstroSat* are expected to be co-aligned it would be necessary to find the offset of each LAXPC detector with respect to the satellite's pointing axis. This offset as well as the field of view of the collimator were expected to be estimated by scanning across the Crab. That should also give a better estimate of collimator misalignment.

For a perfect collimator the dead-time-corrected count rate would vary linearly with pointing offset. The collimator of each detector consists of about 7000 square cells of side 7 mm. The fabrication and mounting of the collimator modules may introduce some level of misalignment between individual cells in the collimator assembly. To produce a more realistic model of the collimator, following Jahoda et al. (2006) we assume that the pointing direction of each cell is randomly displaced from the detector axis. The random offsets are assumed to have a Gaussian distribution centered at the detector axis and with standard deviation, σ_c , which quantifies the imperfection in the collimator. The standard deviation would need to be adjusted to approximate the observed scan profile. The actual collimator may have a misalignment in the mean also, which would again be determined by the scan. The final effective area can only be obtained by cross-calibration with other instruments after launch as described in Section 5.2.

4.3. The Field of View

The field of view of the collimator could not be determined using radioactive sources on the ground. Hence GEANT4 simulations were used to determine it. Each simulation included 10^6 photons of fixed energy that were uniformly distributed over the top of the detector and incident at a fixed

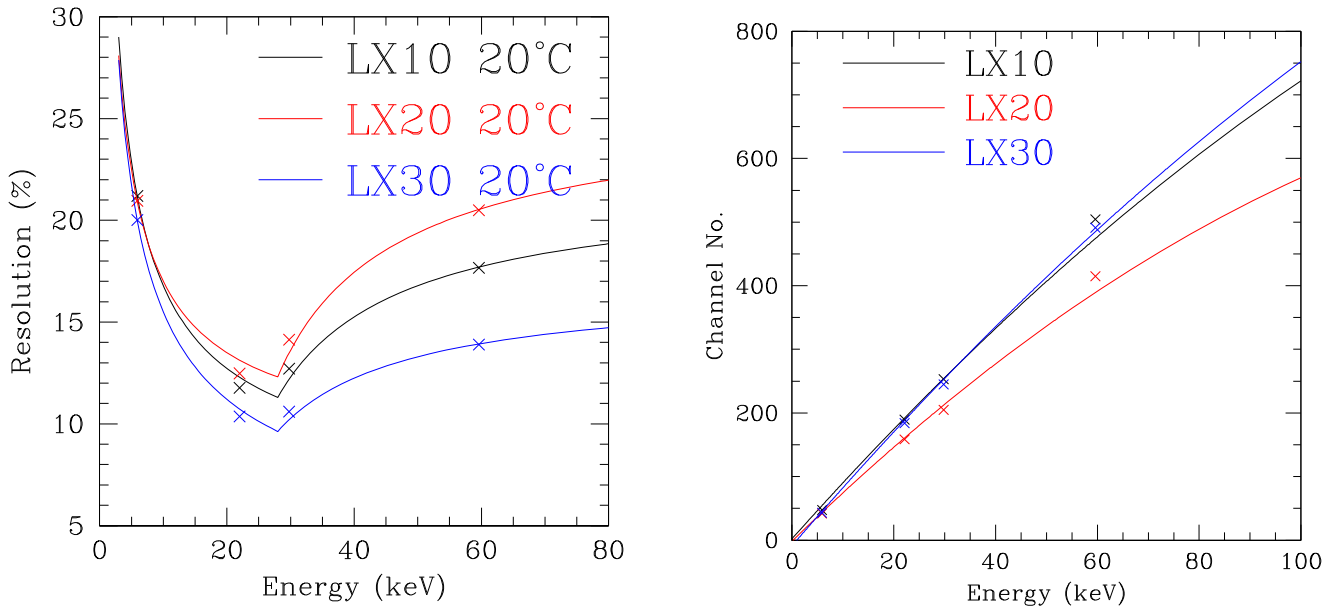


Figure 10. The energy resolution (left panel) and the energy-to-channel mapping (right panel) as determined by fitting the simulated spectrum to the observed spectrum for radioactive sources. The points in the left panel mark the actual value for the four peaks, while those in right panel show the values obtained by fitting the spectrum by a sum of Gaussian peaks.

angle to the detector axis. The number of events registered in the detector was noted for each angle. The secondary particles produced in the collimator are also tracked, and all events that satisfy the selection criteria for the processing electronics were counted. The maximum counts were obtained when the photons were incident normal to the detector surface. The counts at other angles were divided by this maximum number to get the relative efficiency of the detector in different directions. There is some energy dependence in the field of view, because the window support collimator, which is made of aluminum, is almost transparent to high-energy photons. As a result, at high energy the field of view increases marginally. The FWHM of a perfect collimator is $43' = 0^\circ.72$ at 15 keV and $47' = 0^\circ.78$ at 50 keV when measured along the diagonal of the detector. Along the sides of the detector the FWHM turns out to be $50' = 0^\circ.83$ at 15 keV and $54' = 0^\circ.90$ at 50 keV. However, it is unlikely that all cells in the collimator are perfectly aligned in the same direction and it is necessary to include this effect in simulations. On the ground it was not possible to estimate the magnitude of the dispersion in alignment of different cells and hence this was achieved by a scan across the Crab after launch, by comparing the scan profile with simulations with different amounts of dispersion in collimator alignment. The dispersion was assumed to have a Gaussian distribution, and it was estimated that for LAXPC10 the standard deviation of the alignment is about $12' = 0^\circ.2$. This reduces the detector efficiency by about 14%, which affects the effective area also. This estimate of 14% applies when photons are incident perpendicular to the top window; there is a mild dependence on the angle of incidence. Figure 11 shows the contours of constant efficiency for photons of 15 and 50 keV. The red contours that mark the region of half the maximum counts have an FWHM when the scan is taken along the sides of the detectors of $57' = 0^\circ.95$ at 15 keV and $62' = 1^\circ.03$ at 50 keV. These contours are not circular in shape because the cells in the collimator are square.

For other detectors the dispersion in collimator cells is even larger, giving even lower efficiencies. For LAXPC20 the

dispersion σ_c is estimated to be about $19'$, giving a loss of efficiency by about 22%. For LAXPC30 σ is estimated to be about $17'$, giving a loss of efficiency by 18%. It is possible that this dispersion is overestimated because there would also be some contribution from misalignment between the field-of-view collimator and the window support collimator.

4.4. The Detector Background

The detector background arises from the photons and charged particles in space, apart from the X-rays coming from the source. The detector background can be estimated from simulation, if the flux of particles (photons and charged particles) responsible for the background is known at different energies. The high-energy particles interact with the shield and other surrounding material and may produce secondary X-rays or other particles of varying energies. The GEANT4 simulations keep track of all these secondaries. Although the detector is not designed to detect high-energy particles, many of these particles may deposit only a part of their energy inside the detector, thus triggering a valid event in the detector. Simulations include all secondaries produced in the shield, collimators, and aluminum box enclosing the gas and collimator. But simulations do not include other materials surrounding the detector in the satellite, and some differences may be expected as a result. The main purpose of these simulations is to estimate the efficiency with which background events are rejected.

The following are mechanisms for rejecting the background:

1. *The shield.* The shield including the tin shield, aluminum box, and collimators may not allow the particles to pass through. At low energies this is very effective and practically all background events are suppressed.
2. *The detector efficiency.* Since the low-energy particles are shielded from the detector, only high-energy particles will enter the detector volume. At these energies, the detection of photons is fairly inefficient and a large

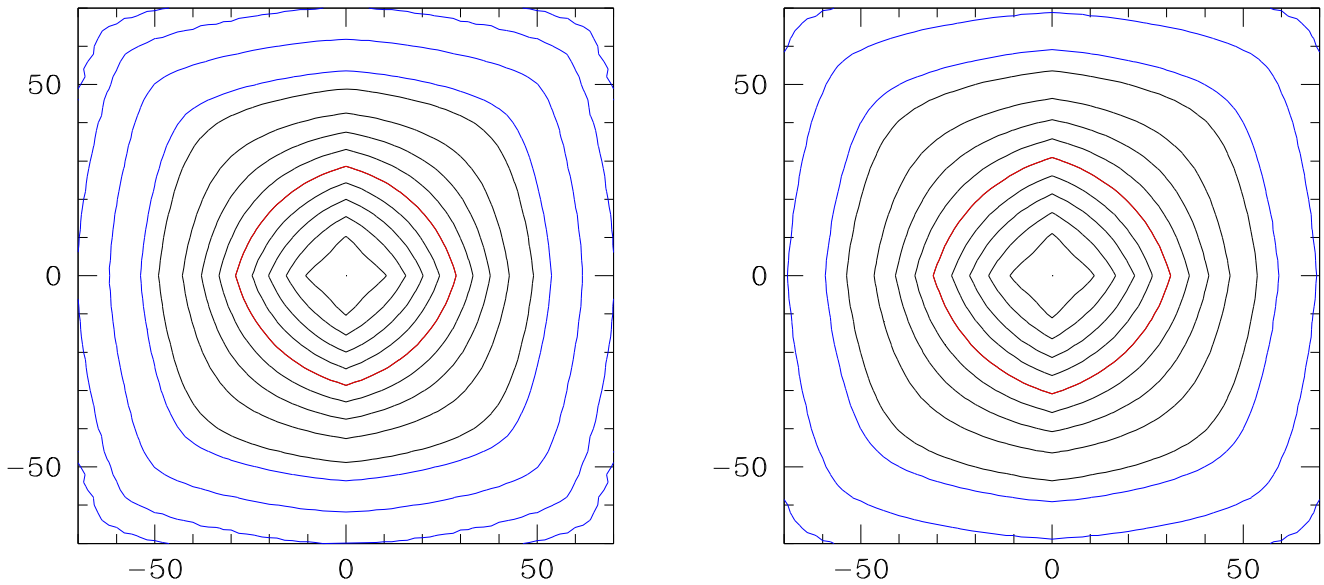


Figure 11. Contours of constant efficiency (relative to the detector axis) are shown as a function of angle from the detector axis for photons of 15 keV (left panel) and 50 keV (right panel). The axes are marked in arcminutes. The red contour encloses the region where count rate is more than half of the peak value and gives the FWHM of the field of view. The black contours are at intervals of 10%, while the blue contours are at levels of 5%, 1%, 0.1%, and 0.01%.

fraction of them will simply pass through the detector without registering an event.

3. *Coincidence.* The logic in the processing electronics rejects all events that trigger more than one anode, except for the xenon K X-ray peak as explained in Section 2. This can reject events due to charged particles.
4. *Veto layers.* Any event that deposits energy in a veto anode is rejected. This would also be effective for rejecting charged particles entering from the sides.
5. *Excess energy.* If the energy deposited in an anode exceeds the ULD of about 80 keV, it will be rejected.

The relative contributions of all these factors were estimated in the simulations. There can be multiple reasons why a given event is rejected. In particular, the last three options can have significant overlap. In the simulations, any event that registers in more than two anodes or two main anodes is accounted for in the contribution from coincidence, while those events that are recorded in two anodes including a veto anode are accounted for in the contribution of veto layers. The excess energy refers to only those cases where at most two main anodes are triggered. The overlap between different options was not estimated in these simulations.

The background flux was assumed to be isotropic and uniform. Only gamma-rays, electrons, and protons were considered separately as the primary particles. Each simulation run consisted of 10^6 events for a chosen particle with energy uniformly distributed in a specified interval. The particles were incident on the virtual surface of a box of size $120 \times 60 \times 80$ cm³ with uniform probability of landing at any point on the surface. The detector was inside this virtual box. The initial direction of incident particles was also considered to be uniformly distributed in the solid angle of 2π that constitutes particles directed into the volume. With a virtual box of this size, it was found that if the shield, aluminum box, and collimator were removed, then on average about 23% of the particles reached the active detector volume ($100 \times 39 \times 16.5$ cm³). This is purely a geometric effect because the active detector is only a fraction of the total volume considered. When

the shielding material is included, the number of particles reaching the detector was much smaller at low energies, but at high energies it approached or even exceeded 23%. The latter is because of secondaries produced in the shield. Nevertheless, because of the various rejection criteria, the number of events actually registered is much smaller. Thus all rates were normalized with this number for consistency.

For each event the total energy deposited in each anode volume was calculated and the rejection criteria outlined above were applied. In order to identify the contribution to background rejection from various measures, all contributions were counted separately. In addition, a count of events rejected by each of the veto layers was kept separately. These include only those events that also triggered one of the main anodes. These are counts that will be added if one of these veto anodes is not functioning, as is the case with LAXPC10.

The results are shown in Figure 12. Photons at energies below about 50 keV are almost completely absorbed by the shield. At higher energies an increasing fraction penetrates through the shield to reach the detector, but at these energies the efficiency of the detector is rather low and a large fraction of these pass through the detector without interacting. For energies above 1 MeV the efficiency of the detector is very low and 70%–90% of the events are rejected because of this. The anticoincidence logic accounts for rejection of up to 30% of events at high energies, while veto layers reject up to 4% of events at high energies. For energies above 10 MeV the anticoincidence is about a factor of 4–7 more effective in rejecting background than veto layers. The fraction of events that pass through all rejection criteria is about 1% or less at all energies. Also shown in the figure is the result if veto anode A10 is not functioning. It can be seen that the increase is typically about 60% at the highest energies and drops to 10%–20% at low energies, where the flux of gamma-rays is likely to be larger.

Similarly, electrons with energies up to 1 MeV are almost completely absorbed in the shield, but the shield is totally ineffective beyond an energy of 10 MeV. For electrons the detector is fairly efficient and only about 20%–30% of events

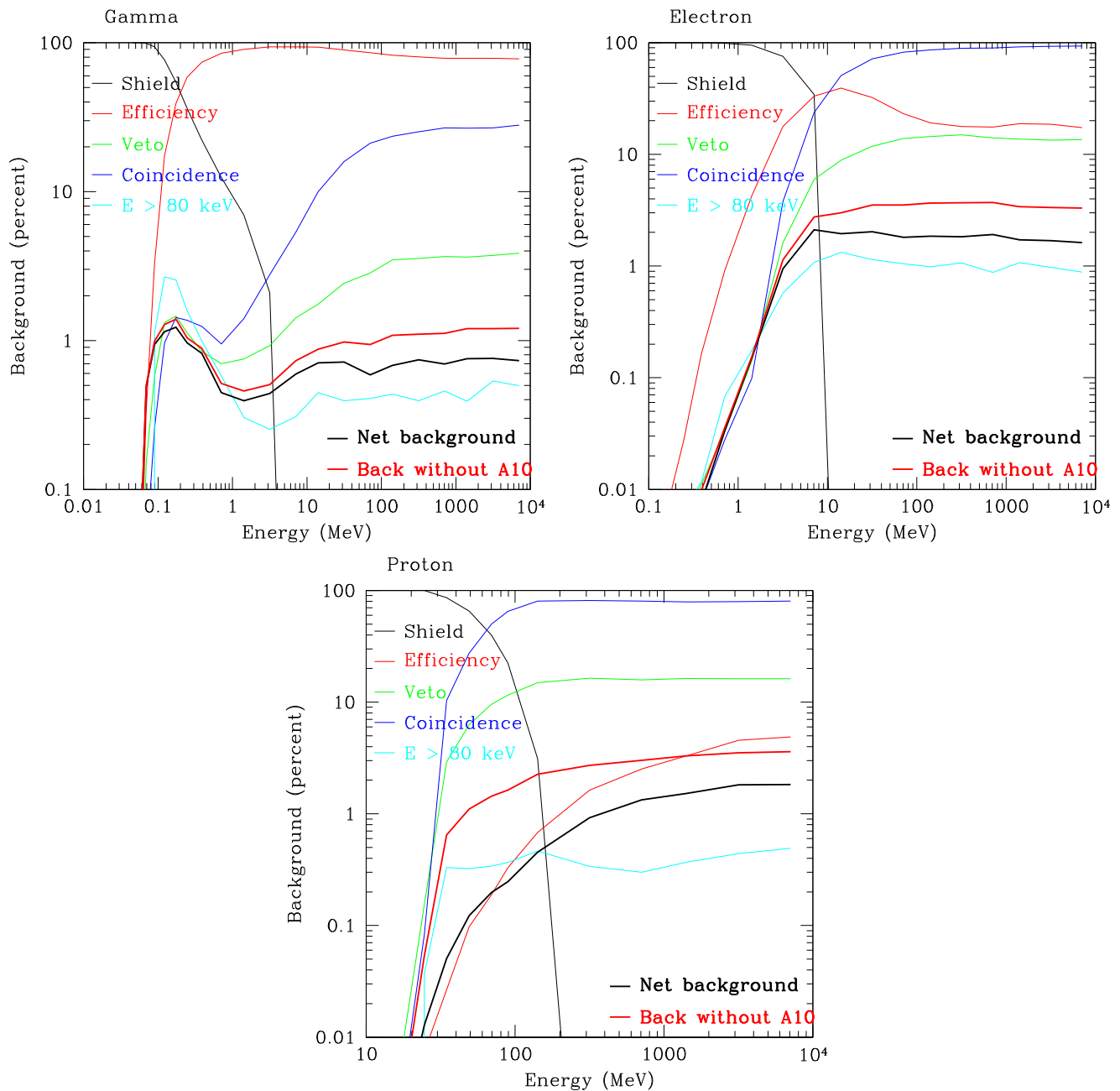


Figure 12. Contributions to background rejection from shield, efficiency, coincidence, veto layers, and excess energy for gamma-rays, electrons, and protons as a function of energy. The net background in the detector with and without veto anode A10 is also shown.

are rejected on that count. However, in this case anticoincidence is very effective and about 90% of the events at highest energies are rejected in that way. The fraction of events rejected by detector efficiency decreases to 10% at 5 MeV. The veto layers account for about 10% of the rejections at high energies and are typically less effective by a factor of 6 than anticoincidence at energies above 10 MeV. The net background recorded by the detector is about 2% of the incident flux at high energies and increases by about a factor of 2 when veto anode A10 is not functioning. At lower energies of 1–10 MeV, where the electron flux is likely to be large, the increase due to A10 not functioning is much less.

For protons the shield is effective up to an energy of 20 MeV; beyond that anticoincidence is the dominant factor in suppressing the background, accounting for over 80% at high

energies. The veto layers account for about 20% of events at high energies. The net background recorded by the detector reaches 2% at high energies, but at these energies the flux of protons should be negligible. At energies below 500 MeV the background is less than 1%. If A10 is not functioning the background could be significantly higher and it drops below 1% at about 50 MeV. The large contribution from A10 at intermediate energies arises because at these energies the protons get significantly attenuated in the shield and veto layer, and after traveling through these they do not have much energy left and hence the event will be registered if the veto anode is not functioning. At higher energies the particles pass through multiple layers and can get rejected through anticoincidence even when one veto anode is not functioning.

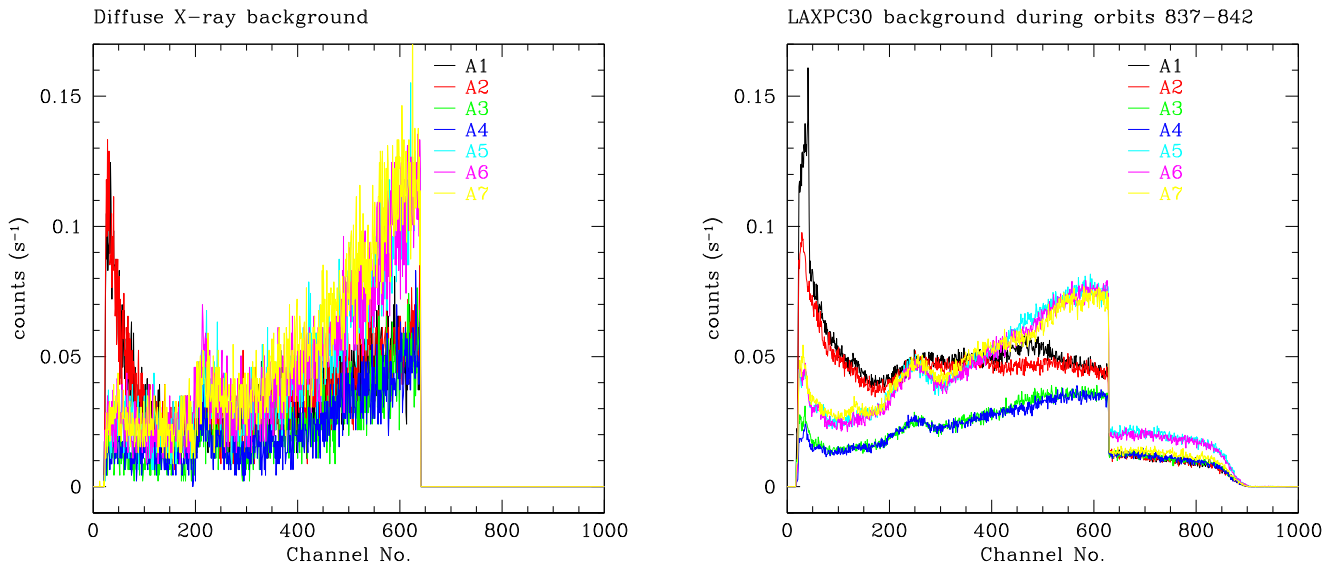


Figure 13. The simulated background from the cosmic X-ray background (left panel) is compared with the observed background in detector LAXPC30 in orbit (right panel).

The charged particle flux in orbit outside the SAA region, where the detector is switched off, is rather small and most of the contribution is expected from cosmic X-ray background. The spectral form of this radiation flux can be approximated by (Mandrou et al. 1979; Schonfelder et al. 1980; Dean et al. 1991)

$$\frac{dN}{dE}(E_\gamma) = 87.4E_\gamma^{-2.3} \text{ cm}^{-2} \text{ s}^{-1} \text{ keV}^{-1} \text{ sr}^{-1}. \quad (5)$$

The resulting background spectrum is compared with the actual background observed in orbit (Figure 13). The simulations suppressed all events with energy exceeding 80 keV, and as a result there are no counts beyond the ULD in the simulated spectrum, while in the observed spectrum the double events contribute to counts in this energy range. It can be seen that the agreement is reasonably good considering the approximations made. More comparisons are discussed in Section 6. It may be noted that a smoothed version of this background spectrum was only used for simulating the LAXPC observations before launch. After launch the observed background is available.

5. Calibration in Orbit

After the launch of *AstroSat* on 2015 September 28, LAXPC detectors were switched on in phases, and on 2015 October 19 the high voltage was raised to the value set during the ground calibration. The first round of gas purification was carried out during 2015 October 20–22. The energy resolution of the detector was estimated using the onboard calibration source in veto anode A8. The results are shown in Figure 14, which compares the spectrum before and after purification. Since the detectors were kept in air for several days before launch some impurities had accumulated in them, thus degrading the energy resolution. Before purification the energy resolutions at 29.8 keV of LAXPC10, LAXPC20, and LAXPC30 were respectively 17%, 12%, and 13%, while after purification they improved to 14%, 12%, and 10%, respectively. After purification, the energy resolution was close to that on the ground. As expected, the gain also reduced after purification. Nevertheless, a second round of purification was performed on

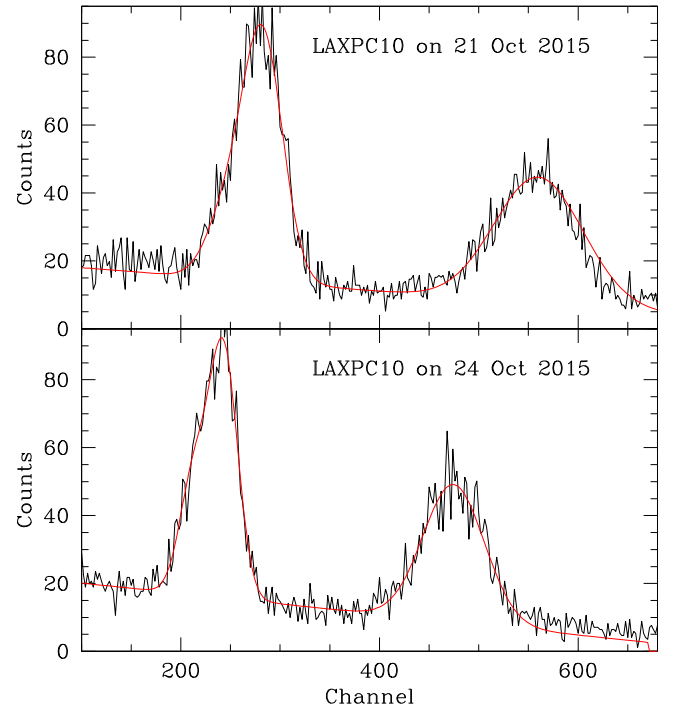


Figure 14. The spectrum in veto anode A8 from the onboard calibration source before (top panel) and after (bottom panel) purification for LAXPC10.

2015 November 22. After this, purification was done on 2016 August 18 for LAXPC10 and LAXPC20.

During the performance verification phase lasting until 2016 March, various sources were observed to calibrate the instruments. Among them was Cas A, which shows an iron line at 6.62 keV (Yamaguchi et al. 2014). The spectrum from observation on 2016 January 4 was fitted to check the peak channel mapping at low energies, and the result is shown in Figure 15. The peak was found at energies of 6.7 ± 0.1 , 6.8 ± 0.1 , and 6.7 ± 0.1 keV for LAXPC10, LAXPC20, and LAXPC30, respectively. The width of the peak was found to be consistent with the expected energy resolution of the detectors. Since the detector response was used in the fit, the

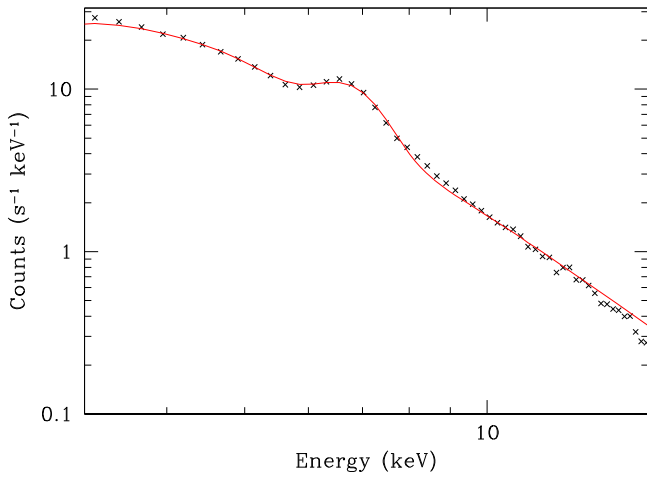


Figure 15. The spectrum of Cas A in LAXPC10 is fitted by a power law and a Gaussian line to get the energy scale. The black points show the observed spectrum, while the red line shows the fitted spectrum.

fitted width was very small as compared to the expected energy resolution of about 20% at this energy. This confirmed that the channel-to-energy mapping used at this energy is within 0.2 keV of its actual value.

All data received after launch have been analyzed using LaxpcSoft software⁸ for analyzing LAXPC data. All results reported in this work have been obtained using this software.

5.1. The Field of View and Alignment

To find the alignment of LAXPC detectors with respect to the satellite's pointing direction we performed a scan across the Crab. The scan was performed in both right ascension and declination at a rate of 0.01 s^{-1} and covered a range of $\pm 3^\circ$ from the nominal position of the source. This exercise was repeated three times, and during each run three scans were done along right ascension and declination. The result obtained during the last run in 2016 February is shown in Figure 16. It can be seen that the detectors do not all show the peak counts at the same time nor when the pointing direction matches the Crab position. Analysis of these data gives the offset for each detector as listed in Table 2. It is possible to choose a pointing direction to maximize the total counts from LAXPC detectors and some observations have been made with such a pointing. However, other instruments on board *AstroSat* have a smaller field of view, and placing the source at the LAXPC efficiency peak would place it far off the axis of some of these.

Apart from the misalignment, the scan profile can also give some estimate of the quality of the collimator, from the rate at which counts fall off with offset from the source. For an ideal collimator the counts should decrease linearly with offset. There is a significant deviation from this linear profile in the region where the count rate is close to maximum as well as where the count rate approaches the background. This departure can be modeled if we assume that not all cells in the collimator are perfectly aligned with each other and that there is a scatter with Gaussian distribution. For the LAXPC10 scan profile, the width of the distribution is found to be about $12'$, while for other detectors it is somewhat larger. Figure 16 compares the observed profile with that expected for an ideal collimator as well as one with a scatter of $12'$. Both the

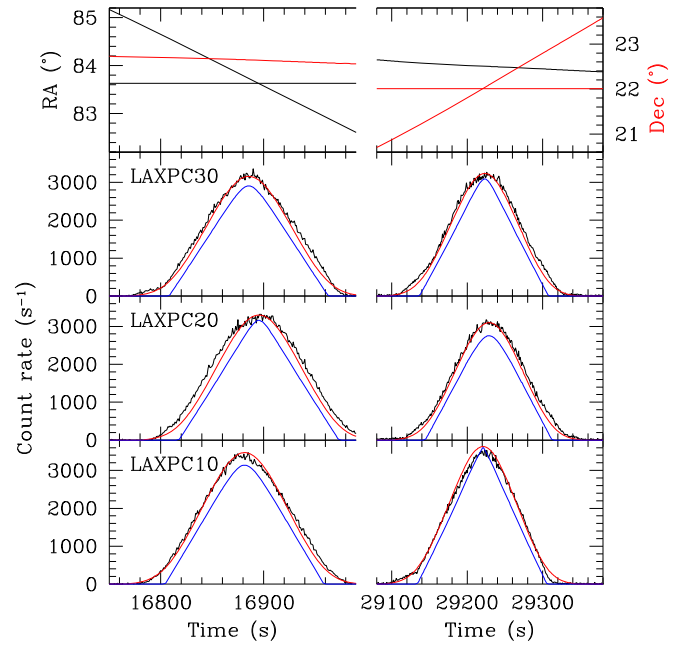


Figure 16. The count rate during a scan across the Crab in right ascension (left) and declination (right) for all three LAXPC detectors. The black lines show the observed count rate corrected for dead-time and background, the blue lines show the count rate expected for an ideal collimator scaled to the observed maximum, while the red line shows the same when a random misalignment by $12'$ in the collimator is included. The top panel shows R.A. (black lines) on the left scale and declination (red lines) on the right. The horizontal lines in the top panel show the coordinates of the Crab.

Table 2

Pointing Direction of Each LAXPC Detector as Determined from the Crab Scan and the Estimated Loss of Efficiency due to Pointing Offset and Collimator Quality

Detector	R.A. (deg)	Decl. (deg)	Offset (deg)	Loss of Efficiency
Crab source	83.63	22.01
LAXPC10	83.78 ± 0.01	22.01 ± 0.01	0.15	21%
LAXPC20	83.63 ± 0.01	22.08 ± 0.01	0.07	25%
LAXPC30	83.74 ± 0.01	22.03 ± 0.01	0.11	23%
Mean	83.72	22.04	0.09	

simulated profiles are scaled to give the maximum count rate that is observed during the scan. It can be seen that the profile for the ideal collimator shown by blue lines in the figure does not match the observed profile and gives a somewhat smaller field of view. In some cases the peak counts in the profile for the ideal collimator are below the observed counts. This is because in these scans the offset angle was never close to zero and at the minimum offset the ideal collimator gives a significant reduction in count rate. For LAXPC10 the profile with a scatter of $12'$ is close to the observed profile considering the assumptions made. The simulations try to account only for misalignment between different collimator cells and not for other imperfections in the collimator, and hence we do not expect a perfect agreement. Nevertheless, for LAXPC20 and LAXPC30 the deviations are somewhat larger, and it appears that these detectors have larger scatter or other imperfections in their collimator. All collimators have an FWHM of the field of view of about $55' = 0.92^\circ$ at low energies when measured along the sides of the detectors. These scans show the total count rate integrated over the entire energy range, but the count

⁸ http://www.tifr.res.in/~astrosat_laxpc/LaxpcSoft.html

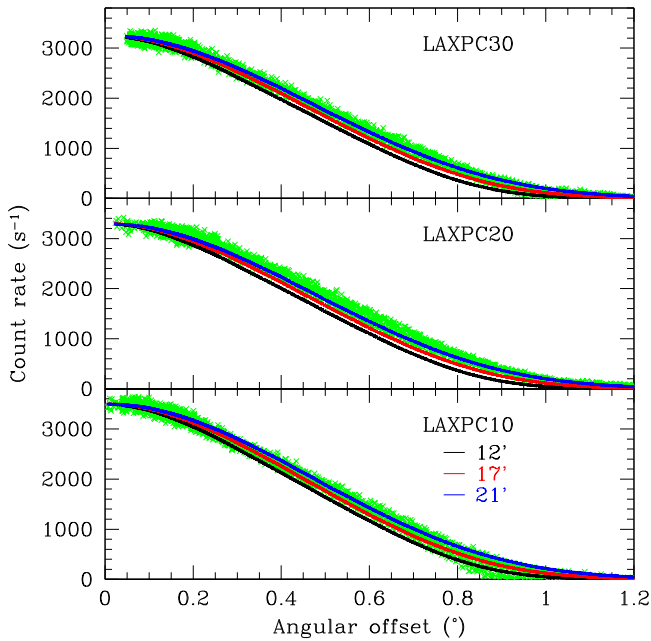


Figure 17. The count rate during a scan across the Crab as a function of the calculated angular offset for the three LAXPC detectors. The green points are the observed counts and other lines are the simulated profiles for various levels of collimator misalignment as marked in the bottom panel.

rate is dominated by low-energy photons and hence the resulting field of view is applicable at low energies.

Figure 17 compares the observed profile during a scan by combining all six scans as a function of calculated angular offset. It can be seen that the profiles of all scans merge into one, which shows that the calculated offset is correct. Further, this figure compares the observed profile with simulated profiles with a few different levels of scatter in the alignment of the collimator. The shape of the simulated profile does not perfectly match the observed profile, and it is likely that there are other imperfections in the collimator that contribute to the differences. Nevertheless, it is clear that LAXPC10 appears to be consistent with lower scatter in the collimator, while the scatter is larger for other detectors, with LAXPC20 having the largest scatter. This is consistent with the estimated effective areas of the three detectors as discussed in the next subsection. It can be seen that the scatter is between 12' and 17' for LAXPC10. It may be noted that this result is only used to estimate the loss of efficiency due to collimator imperfection. The final effective area is estimated by a simultaneous fit with *NuSTAR* observation and does not use this estimate.

We can estimate the field of view at higher energies by considering the counts in different energy bands. If we consider counts in the energy range 40–60 keV the FWHM of the field of view is about $63' = 1^{\circ}05$. Figure 18 shows the results for this energy range and compares them with simulations with a perfect collimator and one with dispersion of 12'.

The offset angle for the detectors ranges from $0^{\circ}07$ to $0^{\circ}15$. For an ideal collimator an offset of $0^{\circ}15$ would reduce the efficiency by about 15%, but considering the scatter in alignment of individual cells at the level that matches observations, the decrease is about 7%. The scatter in the collimator alignment reduces the efficiency by about 15%, which gives a total reduction of about 20% in efficiency for LAXPC10. The reduction is comparable for the other detectors because the smaller offset compensates for larger scatter in the

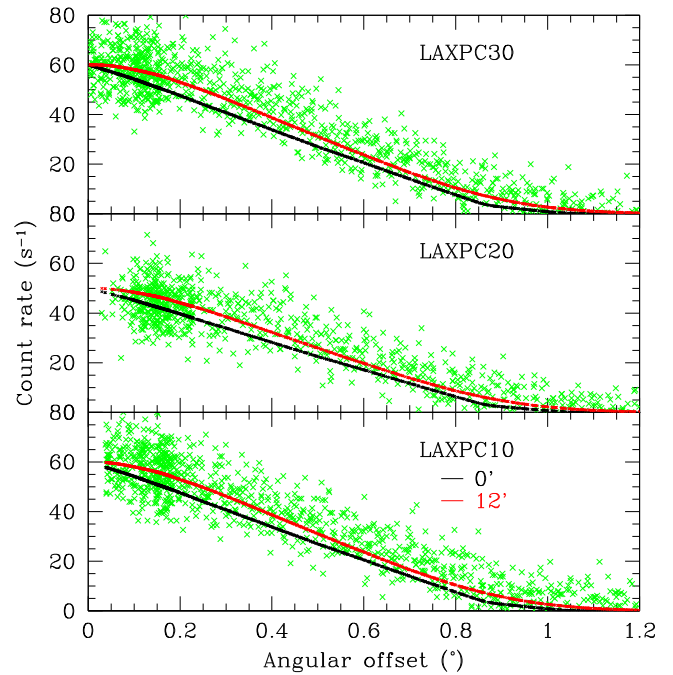


Figure 18. The count rate in the energy range 40–60 keV during a scan across the Crab as a function of the calculated angular offset for the three LAXPC detectors. The green points are the observed counts and other lines are the simulated profiles for two levels of collimator misalignment as marked in the bottom panel.

collimator pointing. Table 2 also lists the estimated loss of efficiency for all detectors due to pointing offset and collimator quality. This is reflected in the effective area considered in the next subsection. It may be noted that these offsets have been obtained with respect to the satellite axis of *AstroSat*. However, not all instruments are perfectly aligned to this axis, and as a result different pointings are used while observing with different instruments. Hence there could be an offset of about $0^{\circ}1$ with respect to the pointing obtained here. As a result, it may be better to keep the normalization of effective area as a free parameter while simultaneously fitting spectra from different detectors or instruments.

5.2. Effective Area

As mentioned in Section 4.2, the effective area of the combined LAXPC detector was expected to be about 8400 cm^2 , assuming a nearly perfect collimator and alignment. From the scan across the Crab we have estimated that the misalignment with respect to the satellite's pointing direction and imperfections in the collimator reduce the efficiency and hence the effective area by about 21% for LAXPC10.

Apart from the collimator imperfection the count rate would also be affected by the dead-time associated with rejected events. This count rate is more or less independent of the source being observed, though it varies during an orbit by about 25%. This rate may be estimated using appropriate counters in BBC mode. However, this rate in orbit is very different from that on the ground and hence it could only be estimated after launch. From the BBC mode data the total counts in rejected events are estimated to be $2000\text{--}2500 \text{ s}^{-1}$. With an estimated dead-time (from the electronics design) of about $35 \mu\text{s}$ for rejected events, this gives a loss of efficiency of

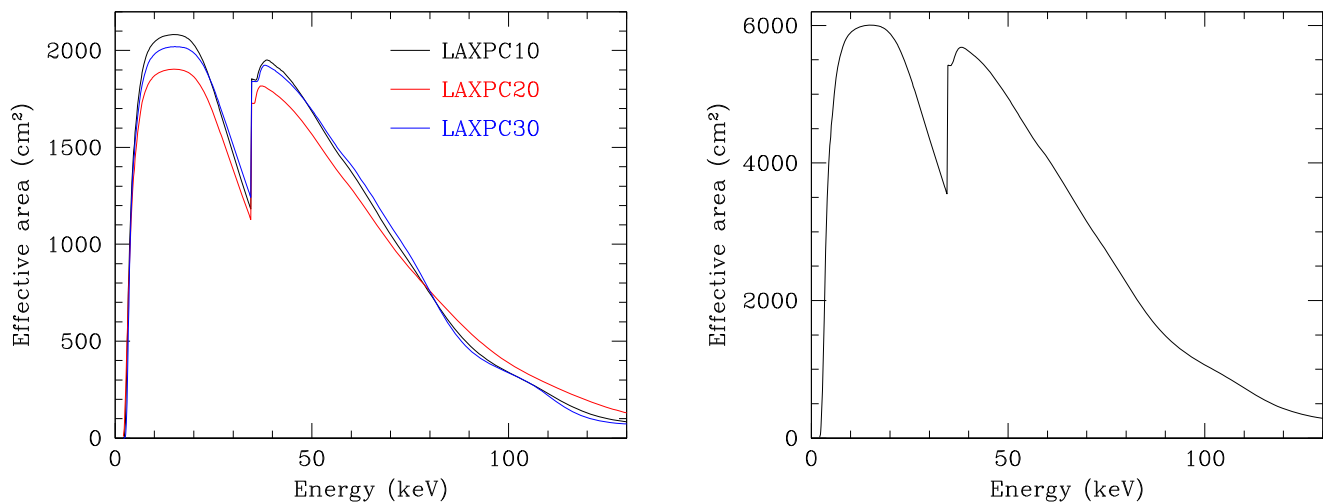


Figure 19. The effective area of the three LAXPC detectors (left panel) as estimated from simulation with scaling determined by observations of the Crab after launch. The right panel shows the effective area when all three detectors are combined.

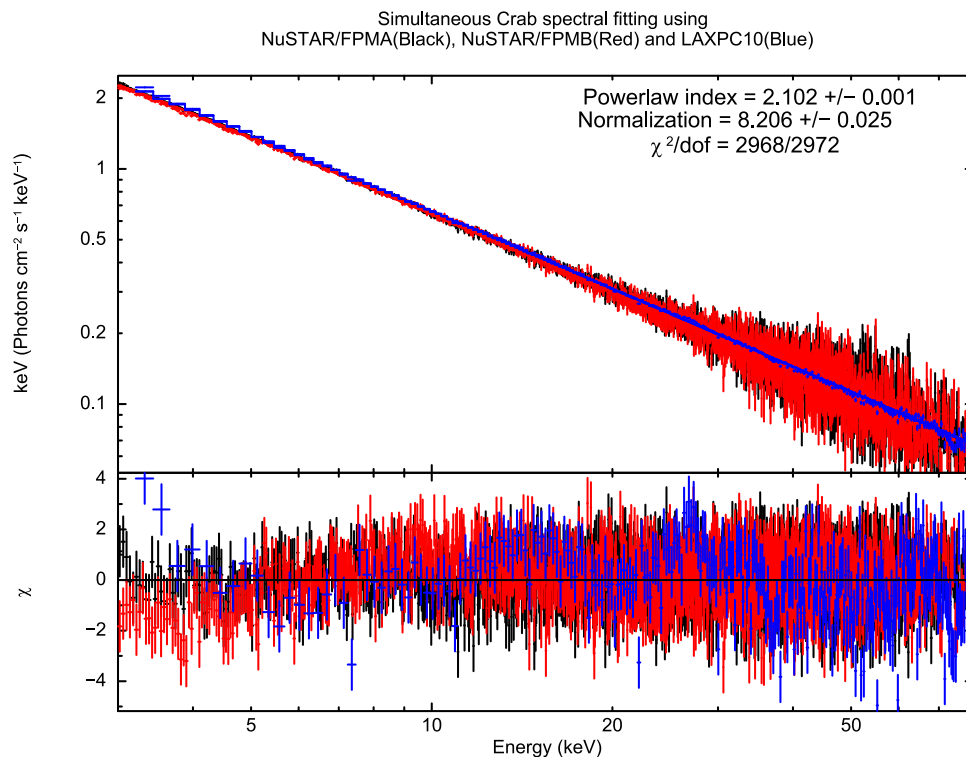


Figure 20. The simultaneous fit to *NuSTAR* and LAXPC10 data for the Crab.

7%–9%. Combining both these factors gives a reduction in effective area by a little over 27% to about 6000 cm².

Figure 19 shows the effective area of the three LAXPC detectors with correcting factor as explained below. The efficiency or the effective area is defined by the probability that a photon of given energy will register a valid event in the detector; the energy deposited may be less than the incident energy, for example, due to Xe K fluorescence X-ray escaping from the detector volume. Thus these photons may not all be detected at the correct energy. The difference between the effective areas of the three detectors is mainly from the collimator quality. For a perfect collimator all detectors show similar effective areas. The total effective area of the three detectors is shown in the right panel. The sharp dip at low

energies is due to absorption in the Mylar window at the top of the detector. The dip around 34 keV is due to reduced absorption coefficient just below the K-edge of xenon. At high energies the efficiency decreases because of a decrease in the absorption coefficient of the gas.

To get a better estimate of effective area for each LAXPC detector, simultaneous observations of the Crab with *NuSTAR* (Harrison et al. 2013) were carried out on 2016 March 31. A simultaneous fit of *NuSTAR* and each of the LAXPC detectors to a power-law spectrum gave the relative normalization of each detector assuming the response matrix for *NuSTAR*. The resulting fit for LAXPC10 is shown in Figure 20. From these fits the relative normalizations with respect to *NuSTAR* of the three LAXPC detectors were calculated to be 0.92, 0.84, and

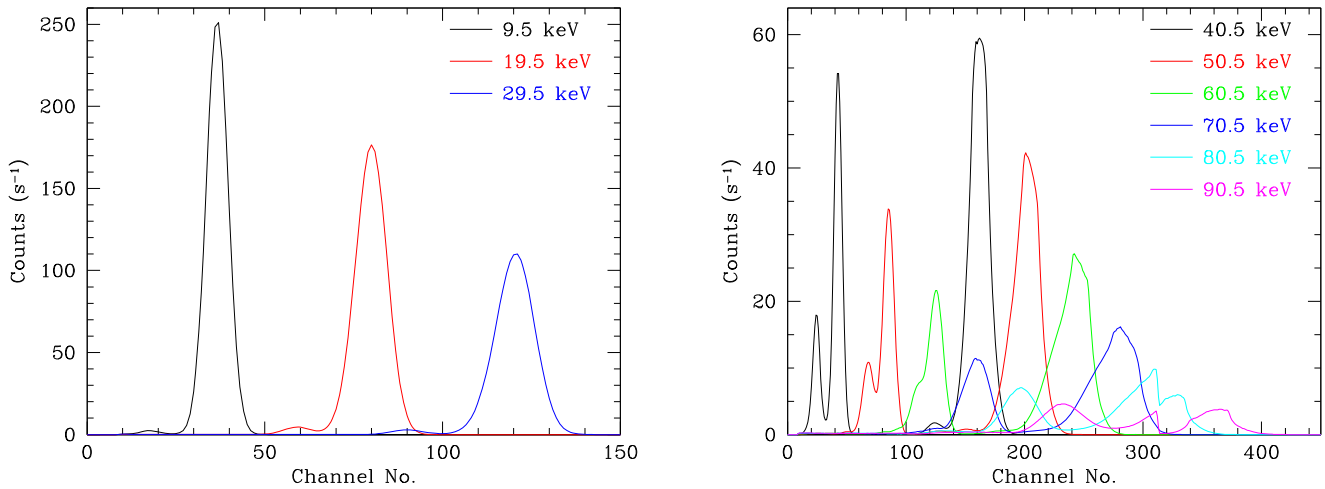


Figure 21. The response of LAXPC30 for a few energies.

0.89, respectively for LAXPC10, LAXPC20, and LAXPC30. The simultaneous fit with *NuSTAR* including 1% systematics in the LAXPC detector response gave a χ^2 of 1.0 per degree of freedom. The effective area of each detector using the normalization as determined above and the combined effective area are shown in Figure 19. The maximum effective area of the combined LAXPC detectors is about 6000 cm² around 15 keV and reduces to about 5600, 4100, and 2200 cm², respectively at 40, 60, and 80 keV. These estimates of effective area are for pointing as determined by the satellite axis. Since the pointing directions are not the same for all observations, there could be an uncertainty in effective area of 5%.

5.3. The Response Matrix

To calculate the response matrix we use GEANT4 simulations with energy resolution and energy-to-channel mapping as obtained in Section 4.1, for photons of fixed energy. We have used 338 energy bins in the range 2.05–145 keV to calculate the response. For each energy we use 10^7 photons incident normally at the top of the detector and distributed uniformly over the area. The efficiency of detection is multiplied by appropriate factor to take care of factors mentioned in the previous section. As explained in the previous section, these factors are determined by a simultaneous fit to the Crab spectrum with *NuSTAR* observations. Figure 21 shows the response of LAXPC30 for a few selected energies. All these are combined into a response file that incorporates the effective area and can be used with the XSPEC package to fit observed spectra.

For energies above the K-edge of Xe we get multiple peaks. The peaks at lower energies are due to escape of Xe K fluorescence X-rays outside the detector. For energies of 40.5 and 50.5 keV the two peaks due to escape of K_α and K_β are resolved. For energies of around 80 keV or above, the main peak may not be complete because a part of the peak may go beyond the ULD, due to finite resolution. However, the counts do not go to zero beyond this limit because the double events are still recorded. At high energies even the main peak due to single and double events may be resolved as the difference increases due to nonlinearity of response. This has not been verified from any source with known energy.

The calculated response matrix was used to fit the spectrum for the Crab taken during 2016 January. Although the overall

fit was good there were some differences around the Xe K- and L-edges. To correct for this the energy-to-channel mapping was locally modified in these regions. Another correction was required to correct for excess events around 30 keV, which come from a gap in the shield. The aluminum box containing the collimator has some ribs of about 1 cm on all sides, and the shield is placed on these ribs. This leaves a small gap between the shield and collimator box (see Figure 1), through which high-energy photons can pass because the aluminum ribs are not sufficient to block them. Only photons arriving in a direction close to the direction of pointing can pass through this gap. Although this region is outside the volume covering the main anodes, the chamber enclosing the gas is larger and these photons can still interact with xenon in this extra volume. Any Xe K fluorescence X-rays emitted in this region can enter the detector volume and trigger the detector. This contribution has been adjusted by matching the Crab spectrum. A typical contribution is about 1% of high-energy photons above the Xe K-edge. This gap was not included in GEANT4 simulations.

This tuned response has been used for all calculations. The fits to the Crab spectrum by a power law for all three detectors with 1% systematics are shown in Figure 22. It can be seen that the fit for all detectors is good to within 2%. Further, the fit for LAXPC10 and LAXPC20 is good even beyond 80 keV, while for that for LAXPC30 deteriorates beyond 80 keV.

The drift in gain of detectors needs to be accounted for while fitting the spectrum using a response matrix as well as while subtracting the background. Since the background spectrum is observed at a different time the gain may not be the same as that during source observation, and it may be necessary to shift the background to the same gain as that during the source observations. The extent of shift required can be obtained by fitting the peak of the calibration source in anode A8. The shift in gain is applied by assuming that the observed shift is due to a change in coefficient e_1 in Equation (3). This assumption may not be correct because other coefficients could also have changed, but it is not possible to determine the change in all coefficients from the shift in the 30 keV peak.

A simple shift in gain will not give the correct spectrum at energies beyond about 35 keV because the logic for adding the double event checks for the energy to be in the interval of Xe K photons. The shift in gain will cause the double events to be missed and it is not possible to account for this while shifting the gain by a linear transformation in energy scale. This limits

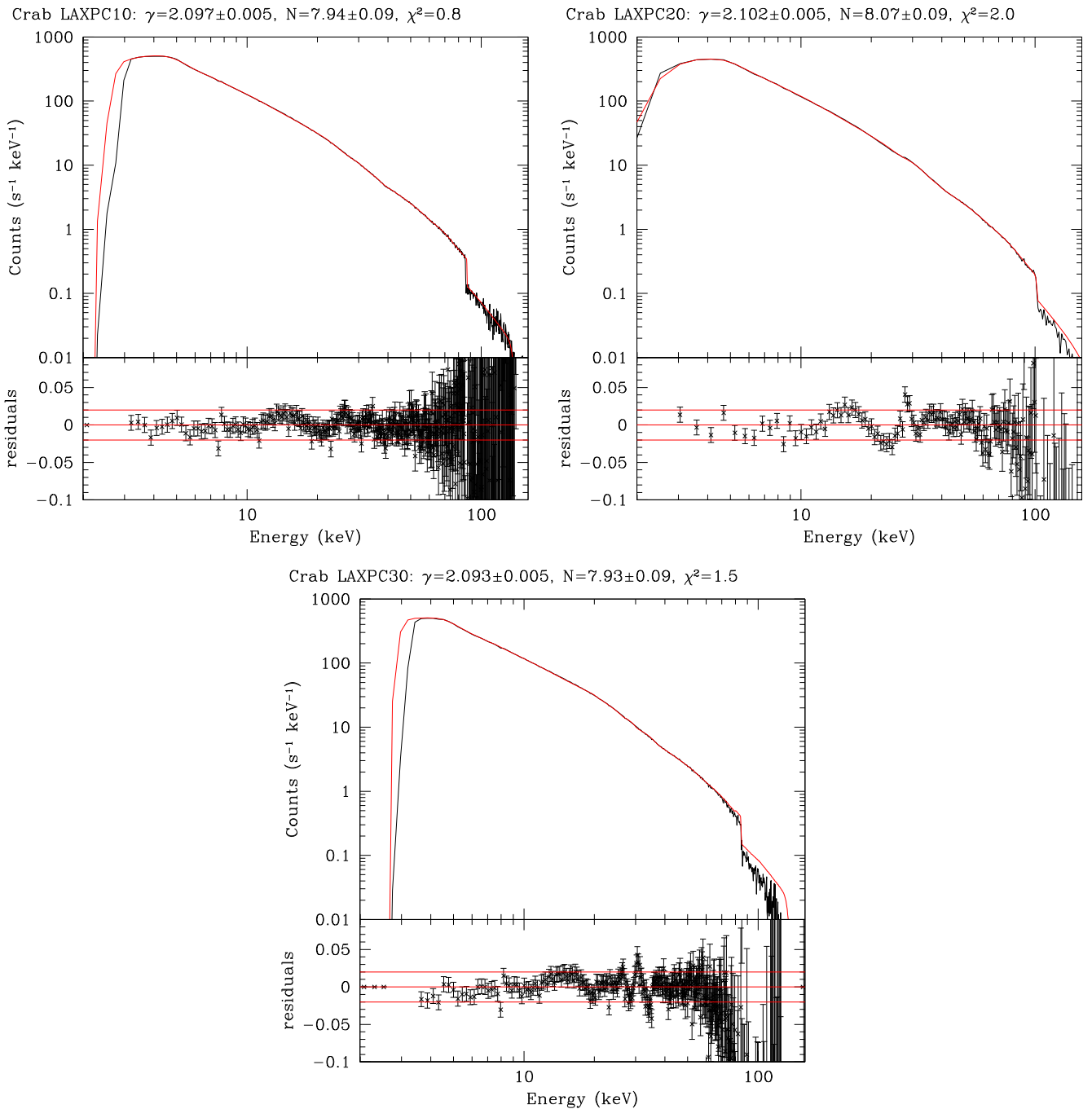


Figure 22. The fit to the Crab spectra for each LAXPC detector using a power-law model with 1% systematics. The black lines show the observed spectra and red lines show the fitted spectra. The lower panel shows the relative difference between the observed and model spectra and the red lines mark the region with differences of 2%.

the ability to correct for a shift in gain between source and background and can introduce features in the resulting spectrum.

Another possibility is to use the spectrum obtained during the Earth occultation during the same orbit as when the source was observed. This ensures that there is no shift in gain between the source and background, but the observed spectrum during Earth occultation is not the same as the real background because the Earth's albedo would also contribute, but this may be the only option if no background observation with nearby gain is available. This issue is discussed in the next section. Once the background-corrected source spectrum is available a

response that has nearby gain can be used to fit the spectrum. The LaxpcSoft software also has an option to shift the background spectrum to align with the source spectrum, and it also identifies the response to be used. It may help to make a finer adjustment in gain by applying a linear transformation to the energy scale, particularly the constant term, e_0 in Equation (3).

5.4. Timing Characteristics

Since the prime use of the LAXPC instrument is for timing studies, the timing characteristics were investigated during ground calibration, and the Fourier transform of the time series

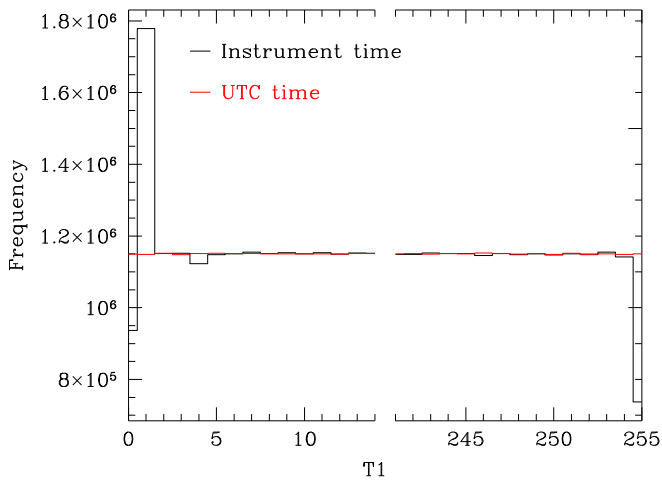


Figure 23. Histogram of frequency of occurrence of different values of the lowest time byte T1 (in units of $10 \mu\text{s}$) during observation of the Crab by LAXPC10 in 2016 January. The black line shows the histogram using instrument time and the red line shows that when UTC time is used.

did not show any unexpected features. After launch this was checked in more detail with additional data for bright sources (Yadav et al. 2016b).

There are some known problems in time tagging of events. When the lowest byte in time, T1, rolls over from FF to 00, the next higher byte, T2, does not increment at the same time. There is a delay of about $20 \mu\text{s}$ between updating the two bytes of time. If an event occurs during this time when two time bytes are updated, and if the count rate is sufficiently high, the apparent time ordering of events may also get disturbed because this event will apparently precede the previous event. A similar problem is also present in the rollover of higher time bytes, though these occur less often and are easier to correct. This problem has been corrected in software, and thereafter all events are correctly ordered in time. However, the distribution of the lowest time byte is not uniform and shows some features as shown in Figure 23. The origin of this effect is not known, but it can result in spurious periodicities if a period of exactly 2.56 ms (frequency of 390.625 Hz) or its multiples is used. The resulting pulse profile will match that shown in Figure 23. The reason for this distribution is not understood but it is independent of time. Since the profile is strongly peaked at one value, most of the power would be in higher harmonics of this frequency; this feature is not seen in the Fourier transform, but it can show up if period-folding is applied. This effect is seen if the instrument time as recorded through the STBG is used. If the arrival times are converted to UTC (red line in Figure 23) the effect goes away because of a slow drift in the STBG clock. We do not believe that this reduces the time resolution because we have obtained the power density spectrum up to a frequency of 50 kHz and it agrees with that expected from a Poisson distribution with dead-time (Yadav et al. 2016b).

After launch a peak around 50 Hz was found in the power density spectrum of bright sources in LAXPC20. This feature is present only in anode A1 and at an energy of less than about 5 keV. It is also found in weak sources with a smaller significance. This has been traced to noise in the amplifier for anode A1. This anomaly was also present during ground tests.

Another source of a possible instrumental feature in the power density spectrum is the calibration source in veto anode

A8. To allow this spectrum to be observed, 1/128 of the events registered in veto anodes are not rejected and get entered in the event mode file. Since the count rate in veto anodes is roughly constant, this gives a peak around 8–11 Hz in count rate from veto anodes. The lower frequency is seen in LAXPC10 where veto anode A10 is disabled and hence the count rate is lower. During observation of bright sources the count rate of veto anodes can be reduced due to the effect of dead-time, thus reducing the frequency at which the peak occurs. For bright sources it is possible that this frequency will show up in the source counts also, and in some cases a weak feature has been seen around this frequency in the power density spectra. This has to be accounted for while interpreting a power density spectrum.

6. The Detector Background

Although the background in the laboratory was very stable, observations in orbit show some variation with time and hence it is necessary to model the background, so that the source contribution can be extracted from any observation. This is particularly important for faint sources. The total number of background counts averaged over an orbit in LAXPC10 is about 260 s^{-1} , while in LAXPC20 and LAXPC30 it is about 200 s^{-1} . The higher count rate in LAXPC10 is because one of the veto anodes is switched off. The variation in background count rate is about 20% around the mean value.

The observed spectrum of the background with counts in all anodes added is shown in Figure 24 for all LAXPC detectors during three different observations. One of these observations was when the satellite was pointing toward the Earth. For comparison a simulated background spectrum calculated before launch is shown in one of the panels and it is clear that the agreement is reasonably good. Since the simulations did not include any contribution from charged particles, it shows that this contribution is small in orbit. There is some difference between the three spectra for all detectors as shown in the right panel. It can be seen that there is some energy dependence in the difference, hence scaling the spectrum by the total counts may not be enough. It is known that the cosmic X-ray background, which is the main contributor to the LAXPC background, has a spatial fluctuation of about 7% (1σ) (Revnivtsev et al. 2003) in the 2–10 keV band. These fluctuations cannot be modeled and they set the flux limit below which faint sources may not be observable. It is not clear how these spatial fluctuations will contribute to the LAXPC background: the background is contributed by particles coming from almost all directions, so many of these fluctuations will be averaged out. Even a bright X-ray source with a hard spectrum that is off-axis can also contribute to the background because the typical rejection efficiency for hard photons above 100 keV is about 99% (Section 4.4), so 1% of these photons can be detected. For example, for the Crab, we would expect a few counts per second when the source is shining on the side of the detector.

To cover some variation, LAXPC has observed the blank sky coordinates listed in Table 3. The table also gives the total count rate observed in each detector. Considering the exposure time, the statistical error in these counts is less than 0.1 s^{-1} and the whole variation can be considered as a systematic error. Some of the variation seen in LAXPC30 counts is due to the shift in gain and decrease in density as discussed in the next section. The gain of the other detectors has also been drifting

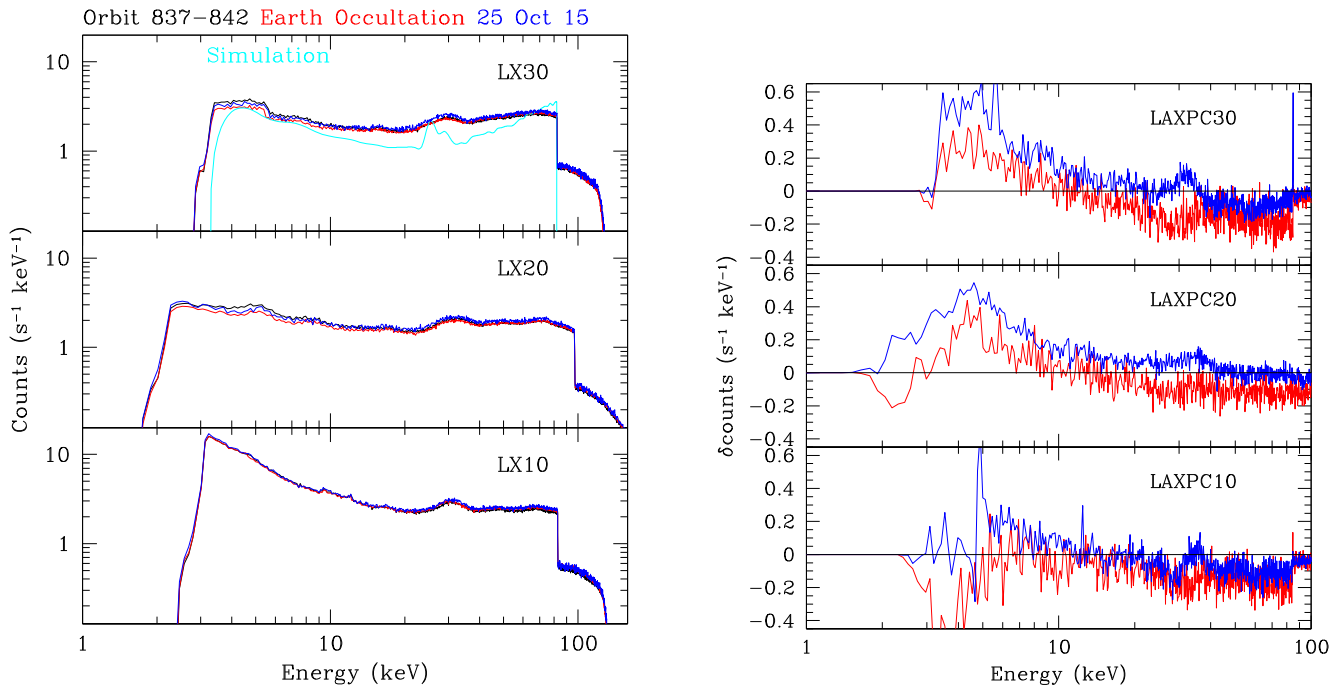


Figure 24. The background spectra for all LAXPC detectors taken at three different times in orbit are shown in the left panel. The black lines show the spectrum during orbits 837 to 842 (2015 November 23), the red lines show the spectrum during the same period when the detectors were pointing toward the Earth, while the blue lines show the spectrum during the first observation on 2015 October 25. The cyan line in the top panel shows the simulated background obtained before launch. The right panel shows the difference between the spectra. The red lines show the difference between the black and red lines in the left panel (difference between background and Earth occultation), while the blue lines show the difference between the black and blue lines (difference between two backgrounds).

slowly and that could account for some of the variations. The background in LAXPC10 appears to be increasing with time; in particular, the count rate after 2016 August is higher than during earlier observations. Table 4 shows the background counts in different layers and different energy bins as observed during 2016 March. Some of the variation in background could be due to variation in satellite position and we attempt to model this. We have tried two models—one based on observed correlation with the count rate of events that exceed ULD, and another based on satellite position. We also tried to model the background variation by using radioactivity induced during SAA passage, but did not find any improvement in the model with this addition and hence we have not included this effect.

6.1. Background Model Based on ULD Counts

Figure 25 shows the variation in background during one day in 2016 March. All the three detectors show an increase in counts as the spacecraft approaches the SAA region. In the SAA region the high voltage is switched off and hence no counts are recorded. The figure also shows the ULD count rate, which measures the number of events that exceed the upper energy threshold. This count rate also shows similar behavior. Further, the increase in the count rate as the satellite approaches the SAA region is not the same in every orbit. It depends on the latitude at that point. *AstroSat* is placed in a nearly circular orbit with an inclination of 6° to the equator. If *AstroSat* is close to 6° S while passing the SAA region, the effect is maximum. On the other hand, when it is close to 6° N, the SAA passage is short and the charged particle flux is also much smaller. The background counts are correlated to ULD counts as shown in the right panel of Figure 25. The correlation coefficient between the two is found to be 0.98, 0.93, and 0.96 respectively for LAXPC10, LAXPC20, and LAXPC30. Since

the ULD counts do not vary too much with source counts, this correlation can provide a simple model for the background. For sources with a high count rate we need to apply a correction for dead-time in the ULD count rate also. To get the resulting model background spectrum the range of ULD counts is divided into four equal bins covering the full range for each detector. The boundary of these bins is marked by vertical lines in Figure 25. For LAXPC30 the background as well as ULD counts are shifted to lower values due to a shift in gain. The background count rate in each of these four bins is shown in Table 5.

The spectra obtained for each ULD bin are shown in Figure 26. For a given source observation, the time is divided into these ULD bins and the background spectrum for these bins is weighted with time spent in the bin to get the resulting background spectrum. The ULD counts need to be corrected for dead-time using the count rate of genuine events. This method is sensitive to the shift in gain that affects the ULD counts. If the gain shifts to the positive side some events at the high-energy end will go beyond the ULD and the observed count rate will reduce while the ULD count rate will increase, thus affecting the observed correlation. For LAXPC30 the ULD counts have reduced significantly due to a leak and it is not possible to use this model. This background model does not give the background count rate as a function of time, but only corrects for the average background spectrum during an observation. Hence, it cannot be used to obtain the light curve for source counts.

6.2. Background Model Based on Satellite Position

Since the SAA region is located mainly just south of the equator, the background counts depend on both longitude and latitude. A background observation over one day is expected to

Table 3
Blank Sky Coordinates Observed by LAXPC

Target	R.A. (deg)	Decl. (deg)	Date	Exposure (s)	Count Rate (s^{-1})		
					LAXPC10	LAXPC20	LAXPC30
Sky9	237.22	46.92	2015 Oct 19	37465	195	205	195
Sky5	57.37	-47.09	2015 Oct 21	18643	199	186	180
Sky2	136.35	26.46	2015 Nov 23	43326	239	197	192
Sky8	236.80	70.35	2016 Jan 5	12124	259	190	193
Sky9	237.22	46.92	2016 Mar 14	48250	263	201	114
Sky9	237.22	46.92	2016 Mar 23	48062	263	205	202
Sky9	237.45	47.26	2016 Aug 16	39297	288	210	160
Sky5	57.37	-47.09	2016 Aug 30	33809	290	212	161
Sky6	77.42	12.42	2016 Sep 16	47162	296	212	143
Sky10	321.13	-48.53	2016 Oct 16	42760	293	217	137
Sky6	76.13	12.71	2016 Dec 03	45812	285	204	150
Sky3	129.32	-27.97	2016 Dec 25	36986	280	205	117
Blank Sky	183.47	22.81	2017 Jan 23	45312	293	206	130
Sky8	237.33	70.20	2017 Feb 13	52701	286	209	129
Blank Sky	183.47	22.81	2017 Apr 13	59094	290	191	111
Blank Sky2	180.01	35.19	2017 May 29	60314	277	189	094

Table 4

Background Count Rates in LAXPC Detectors in Different Layers and Energy Bins during 2016 March

Layer	Energy bin (keV)	LAXPC10 (s^{-1})	LAXPC20 (s^{-1})	LAXPC30 (s^{-1})	Total (s^{-1})
All	All	264	205	202	668
1	All	92.3	68.0	64.5	224.8
2	All	49.5	36.0	35.8	121.3
3	All	31.1	34.0	34.5	99.6
4	All	47.4	33.5	33.9	114.8
5	All	43.7	33.7	33.4	110.8
All	3-20	95.7	34.4	34.9	165.0
1	3-20	35.6	17.0	17.3	69.9
All	20-40	47.5	35.7	38.3	121.5
All	40-80	102	112	107	321
All	3-80	246	184	180	606

cover most of the region where the detector is not switched off. Thus using such an observation it is possible to fit the 2D dependence using product B-spline basis functions, and this model was used. There is also some variation with altitude. Although the orbit of *AstroSat* is nearly circular there is a variation of about 15 km in altitude during the orbit, which may be enough to give some variation in background counts. Hence we also attempted to fit in three dimensions using product B-splines. Some regularization was also applied while calculating the fits (Antia 2012). However, the fitted background did not show any significant improvement over the two-dimensional fit. The fitted backgrounds for all three detectors are shown in Figure 27 for observations during 2016 March. Since the detectors are off during SAA passage that region is excluded from the figure. The residual obtained after subtracting the fitted background from the observed value is shown in Figure 28.

Until 2016 August 4 the SAA region was defined to be between the longitudes of -110° and 0° (or from 250° to 360°). It was felt that this includes some region in the north where the charged particle flux may be low enough for the detectors to be operated. Hence, a modified definition based on an SAA model was implemented that accounted for the latitude dependence, and the entry to SAA was defined to be the point

where longitude equals $-110^\circ + 4(\text{latitude} + 6^\circ)$. With this change in definition of the SAA region, a revised background model is needed, and this was obtained from observations of background on 2016 August 16; the results are shown in Figure 29. There appears to be some region in the north where background counts are quite large and it is necessary to eliminate this region from the good time interval to get a reliable model for the background. There is also some variation in the average background count rate between the two background observations, mostly because of the shift in gain of the detectors between the two observations (see Table 3 and Section 7).

This model gives the total background counts at any position of the spacecraft. For source observation, we take the mean count over the period when the source was observed and scale the background spectrum to this mean count. Apart from the spectrum this model also gives the background counts at any time, and this can be subtracted from the total light curve to get the source contribution. In most regions the background model agrees with actual counts to within 2%. But there is some unexplained variation with a period of slightly less than a day and an amplitude of a few counts per second, which is not modeled. The origin of this periodic variation is not known. The background spectrum obtained from this model does not account for the variation in the spectrum over the observed period. It only accounts for the total count rate, which is used to scale the spectrum.

In order to obtain the fits to the background we need observations covering the entire range in longitude and latitude, which requires observations spanning at least one day. Apart from this we also require that the entire range of longitude and latitude is covered during the time when the satellite is not pointing toward the Earth. Some pointing directions are excluded by this criterion at a given time. For example, the observation of Sky5 during 2016 August 30 did not include any region with latitude greater than 4° and hence cannot be used to obtain the background fit.

6.3. Background from Observation during Earth Occultation

During observations of all sources with declination less than about 60° there are periods during orbit when the source is

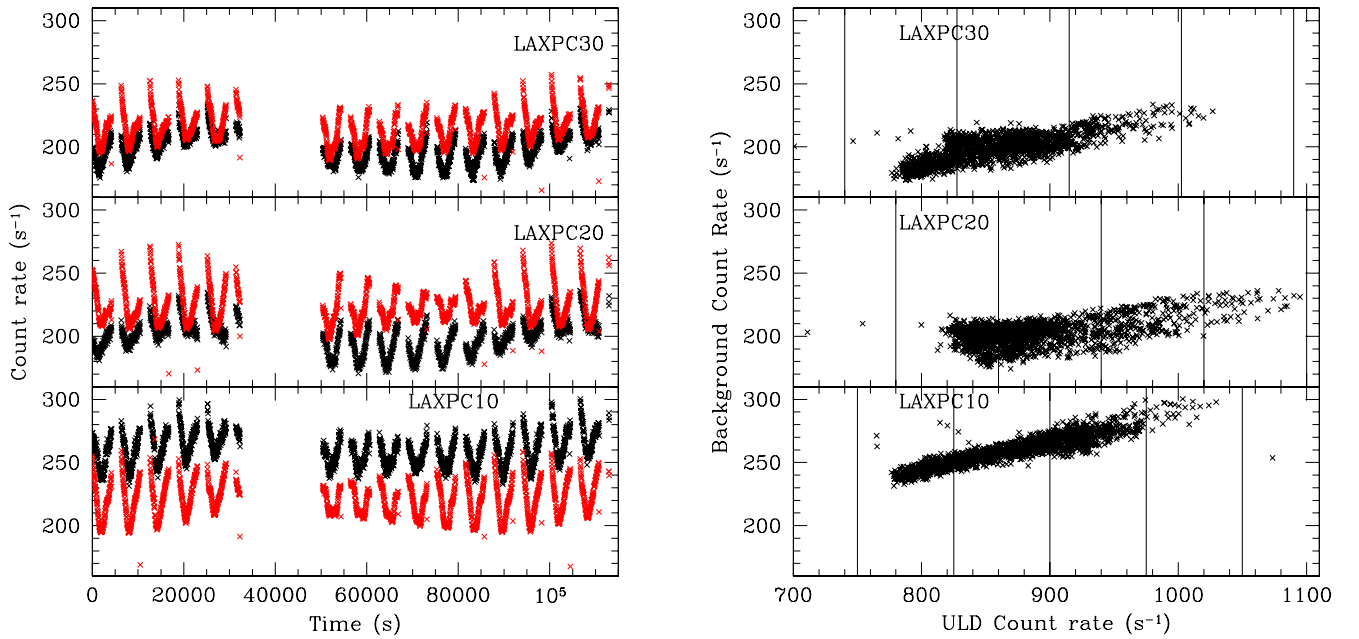


Figure 25. The left panel shows the variation in count rate over about one day of background observation (black points) in 2016 March. The ULD count rate (red points) is also shown. The ULD rate has been divided by a factor of 4 to fit on the same scale. The right panel shows the two count rates plotted against each other. The vertical lines mark the four bins used to generate background spectra.

Table 5
Background Count Rate in Different ULD Bins for Each Detector on 2016 March 14

Detector	ULD-1 (s^{-1})	ULD-2 (s^{-1})	ULD-3 (s^{-1})	ULD-4 (s^{-1})
LAXPC10	248	262	275	299
LAXPC20	201	203	214	230
LAXPC30	190	204	217	230

occulted by the Earth and the satellite is facing the Earth. The source will not be visible during this period but the observed spectrum would not be identical to normal background because there would be some contribution from the Earth’s albedo and the Earth would block the diffuse X-ray background that goes directly through the collimator. The advantage of using the spectrum during the Earth occultation as a background is that a separate background observation is not required, and more importantly it ensures that there is no shift in the gain between the source and background spectra. Hence we have tried to study the difference between the true background, as obtained when the satellite is pointing in a direction where there is no X-ray source detectable by LAXPC, and the Earth occultation spectrum obtained when the satellite is pointing toward the Earth. This can be conveniently done during the background observations because most of the background regions observed are at latitudes low enough to have Earth occultation.

Figure 30 shows the ratio of counts during Earth occultation and background during five different background observations for all three LAXPC detectors. It can be seen that, particularly at low energies, the ratio is far from 1 for LAXPC20 and LAXPC30. LAXPC10 shows a different behavior because one of its veto anodes (A10) has been disabled. It is clear that the use of Earth occultation as background can introduce significant error at low energies, particularly for faint sources. However, in some cases it may be preferable to use this, particularly for LAXPC30 because its gain shifts significantly

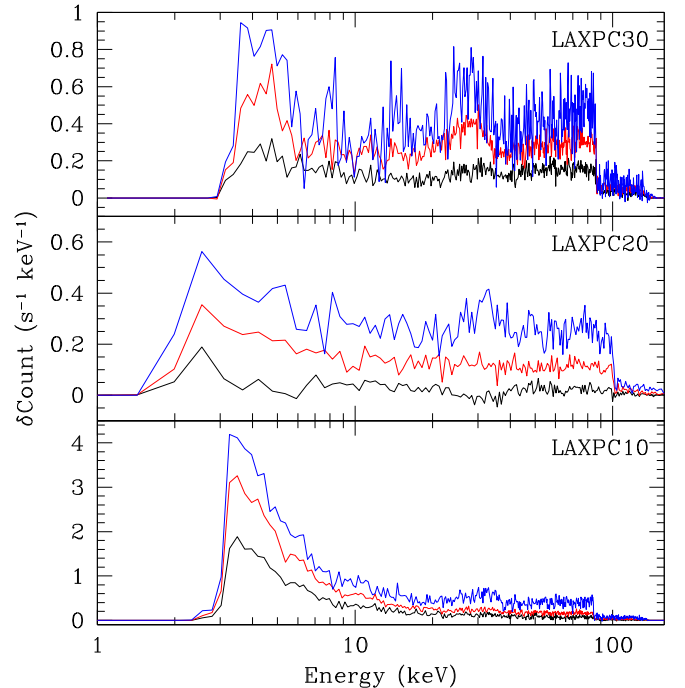


Figure 26. The background spectra in different ULD bins for the three detectors as observed during 2016 March. For each detector the figure shows the difference in count rate with respect to the lowest ULD bin. The black lines show the difference ULD2 – ULD1, the red lines show ULD3 – ULD1, while the blue lines show ULD4 – ULD1.

during a day and it is difficult to account for that from independent background observation.

7. Long-term Performance of LAXPC in Orbit

The health parameters of the detectors, such as the temperature, high voltage, and various energy thresholds, are monitored regularly. The temperature has been maintained at

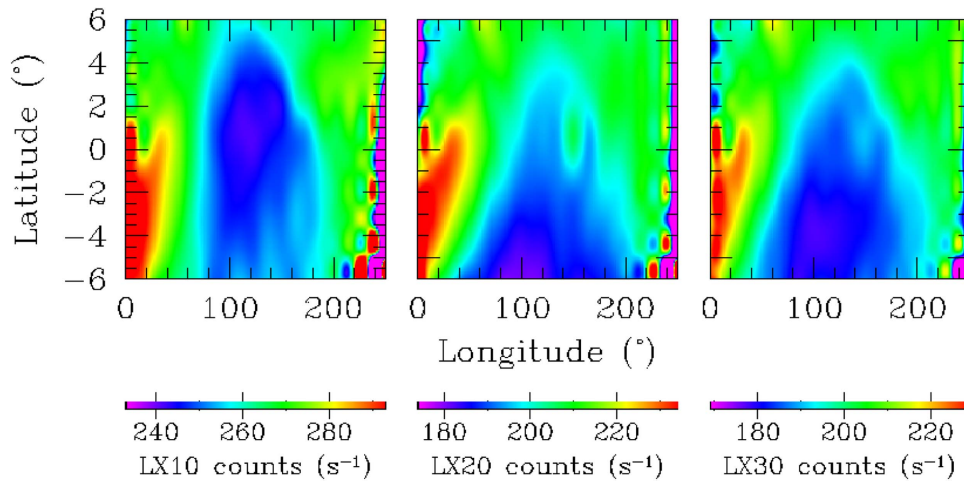


Figure 27. The background count rate as a function of latitude and longitude in all detectors as observed during 2016 March.

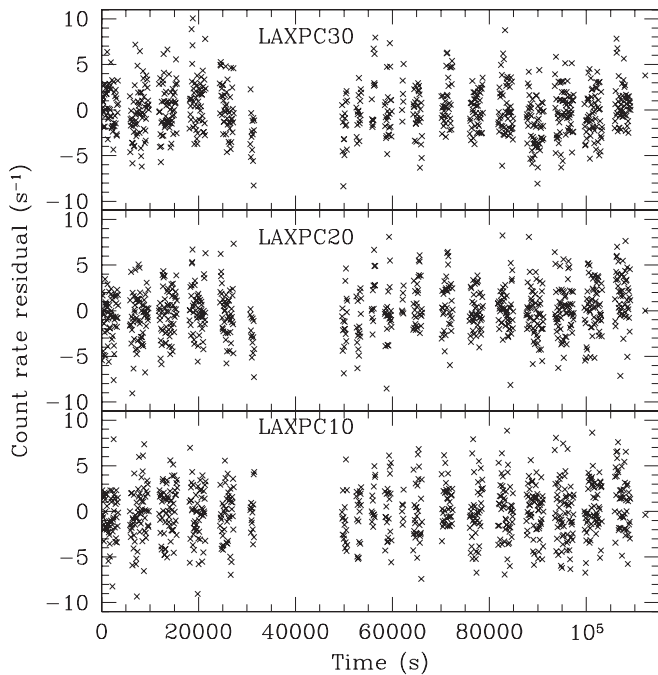


Figure 28. The residual in the background after subtracting the fit for observation during 2016 March.

$18^{\circ}\text{C} \pm 2^{\circ}\text{C}$ for LAXPC10 and LAXPC20, and at $22^{\circ}\text{C} \pm 2^{\circ}\text{C}$ for LAXPC30. The energy thresholds have also remained steady, except for one instance when on 2016 April 19, the lower level discriminator of LAXPC10 was accidentally changed. This was corrected within a day. The high voltage has held steady, but as explained below, it is being adjusted from time to time to maintain the gain of detectors. To monitor the long-term stability of detectors the position and energy resolution of the 30 and 60 keV peaks in the veto anode A8 from the onboard radioactive source are monitored regularly. Figure 31 shows the positions and energy resolution of the two peaks as a function of days after launch of *AstroSat*. Some of these variations are due to purification of gas and adjustment of high voltage. Table 6 shows the times when the gain was adjusted. The gain in LAXPC30 has been constantly shifting due to a suspected leak. As a result, the high voltage is regularly adjusted for this detector. The 30 keV peak had

shifted by up to 85 channels (out of 1024 channels) before the high voltage was adjusted downward for the first time on 2016 March 17 after the leak was verified. During 2015 October–December the shift in gain was small and similar to that in LAXPC10. During the first week of 2016 January, the rate of shift in gain in LAXPC30 started increasing. This shift in gain has to be accounted for in the response matrix, and response matrices have been generated for different shifts. Figure 32 shows the position of the 30 keV peak on a magnified scale.

Unfortunately, the onboard pressure gauge does not have adequate sensitivity to get an accurate measure of the leak. Hence, we attempted to estimate the density of the gas using the ratio of count rates in different layers as was done on the ground (Section 4.1). For this purpose we use counts in the range 20–24 keV. Since the background spectrum is essentially flat we have to subtract the background from the source spectrum for this purpose, and we also need a bright source with a soft spectrum to get sufficient counts in all layers. We found Cyg X-1 to be a suitable source for this purpose. Following a procedure similar to that on the ground as described in Section 4.1, we take the ratio of counts in the energy interval 20–24 keV for different layers with respect to the top layer and minimize the function

$$F_x(\rho) = \sum_{i=2}^5 (r_i - s_i)^2, \quad (6)$$

where r_i is the ratio of counts in the i th layer to counts in the top layer in the observed spectrum and s_i is the same ratio in simulations with a prescribed density. Figure 33 shows the function defined above for five different observations of Cyg X-1 on 2016 January 8, April 29, June 1, July 1, and October 9. The density is shown in units of the initial density estimated on the ground to estimate the loss due to leakage. This appears to indicate that the density in LAXPC30 is decreasing by about 5% of its original value every month and has now reached about 30% of the original value. During the first observation on 2016 January 8, which was the time when the leak became significant, the density is comparable to that estimated on the ground. This gives us some confidence in this estimate. Also, no observations before launch showed any significant shift in gain.

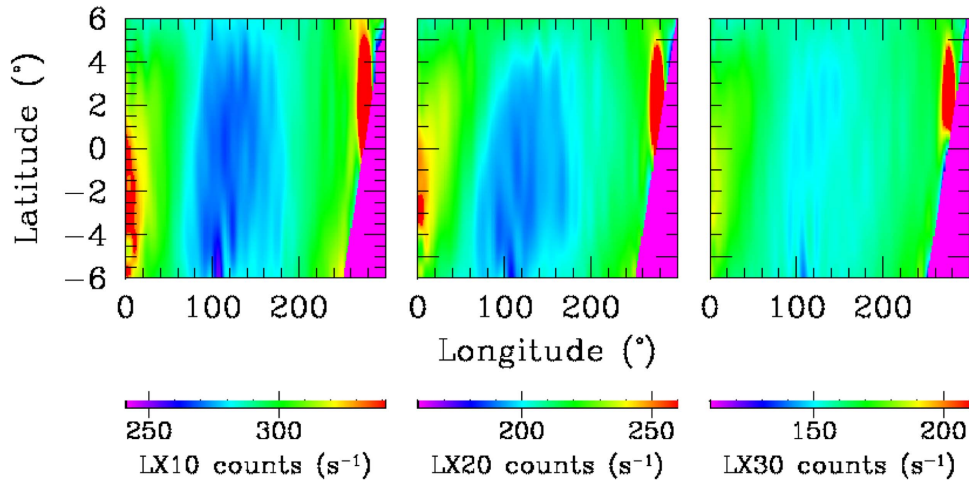


Figure 29. The background count rate as a function of latitude and longitude in all detectors as observed during 2016 August after the SAA criterion was changed.

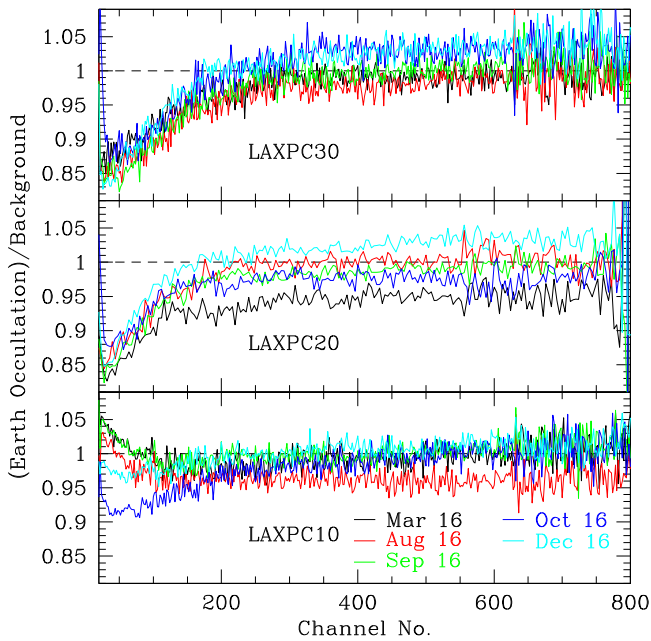


Figure 30. The ratio of counts during Earth occultation and background observations during different times.

Since the detector response depends on density, the response matrix has been generated for values of density differing by steps of 5% of the original value. These responses have been used to fit the observed spectra for some of the sources to find the density that gives the best fit. That also gives an independent estimate of density that agrees with the previous estimate. An estimate of the density in LAXPC30 has been obtained by fitting the Crab observations during different times between 2016 February and 2017 February. These estimates are comparable to those obtained using Cyg X-1 observations described above and also with pressure estimated from the pressure gauge as shown in Figure 34. Since the absolute calibration of the pressure gauge is not reliable, we have divided all values by the maximum value observed and we assume that pressure is proportional to the density. Figure 35 shows the effective area of the detector with different densities. It can be seen that at high energies the effective area has been steadily decreasing with density. But at energies of less than

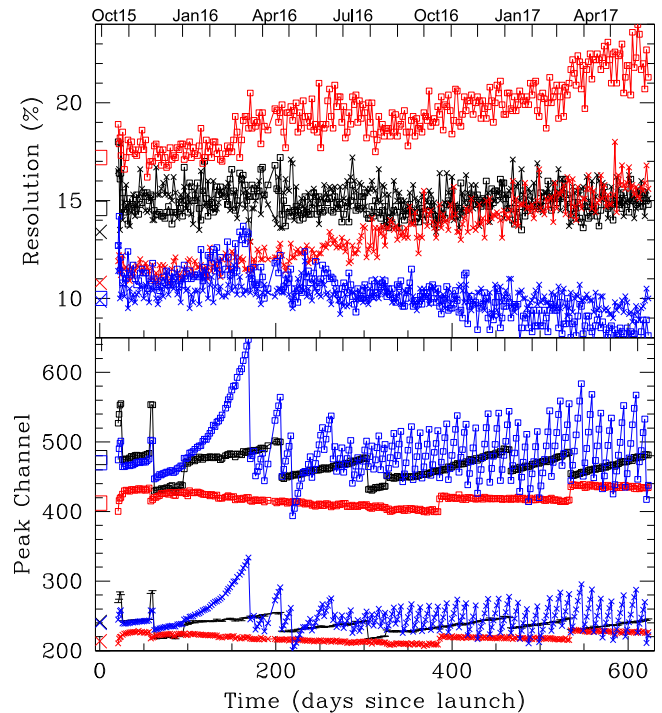


Figure 31. The positions and energy resolution of the 30 keV peak (crosses) and the 60 keV peak (open squares) as a function of time for all detectors as obtained from the veto anode that has the calibration source. The black, red, and blue lines respectively show the results for LAXPC10, LAXPC20, and LAXPC30. The time is measured in days from the launch of *AstroSat* on 2015 September 28. The point at $t = 0$ shows the value observed during ground calibration.

10 keV, there is little difference even when the density is 10% of the original value.

Figure 32 shows that the gain in LAXPC10 is also shifting steadily upward, though at a much smaller rate than LAXPC30. The rate was about 0.15 channels per day, which is more than 20 times smaller than that for LAXPC30. This rate has also increased to about 0.25 channels per day since 2016 September. This could also be due to a very fine leak, which has been there at least since launch. If this rate is held, the detector should function for several years. No change in density or pressure has been detected in LAXPC10 until now. Considering the rate of change of gain and density in

Table 6
High-voltage Adjustments Carried out on LAXPC Detectors

Detector	Operation	Date	Voltage (V)	Remarks
LAXPC10	HV	2015 Oct 19	2369 ± 15	First on
LAXPC10	HV	2015 Oct 23	2334 ± 15	After purification
LAXPC10	HV	2015 Oct 24	2345 ± 15	After purification
LAXPC10	HV	2015 Nov 28	2331 ± 15	After purification
LAXPC10	HV	2016 Jan 2	2341 ± 15	...
LAXPC10	HV	2016 Apr 21	2328 ± 15	...
LAXPC10	HV	2016 Jul 27	2310 ± 15	...
LAXPC10	HV	2017 Jan 6	2300 ± 15	...
LAXPC10	HV	2017 Mar 15	2290 ± 15	...
LAXPC20	HV	2015 Oct 23	2608 ± 15	First on
LAXPC20	HV	2016 Oct 17	2618 ± 15	...
LAXPC20	HV	2017 Mar 15	2628 ± 15	...
LAXPC30	HV	2015 Oct 19	2331 ± 15	First on
LAXPC30	HV	2015 Oct 23	2317 ± 15	After purification
LAXPC30	HV	2015 Oct 24	2321 ± 15	After purification
LAXPC30	HV	2015 Nov 28	2314 ± 15	After purification
LAXPC30	HV	2016 Jan 2	2320 ± 15	...
LAXPC30	HV	2016 Mar 17	2260 ± 15	...

Note After 2016 March LAXPC30 gain is adjusted regularly when required. HV = high voltage.

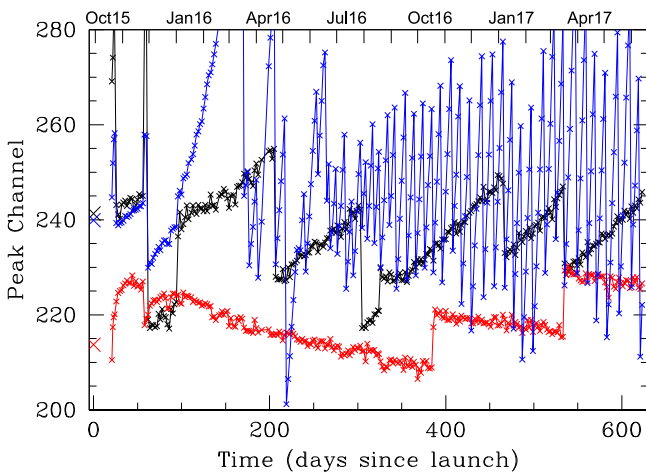


Figure 32. The position of the 30 keV peak as a function of time for all detectors. The black, red, and blue lines respectively show the results for LAXPC10, LAXPC20, and LAXPC30. The time is measured in days from the launch of *AstroSat* on 2015 September 28.

LAXPC30, it can be estimated that the observed shift in gain in LAXPC10 could be due to a 2%–3% reduction in density. This is at the limit of the sensitivities of techniques employed here. The fit to the Crab spectrum observed during 2017 January, with a response using the original density, was very good and there is no indication of any reduction in density. For LAXPC20 the gain has been slowly shifting downwards, which is the behavior expected as a result of impurities accumulating in the detector. The resolution of this detector is also deteriorating with time. The gas purification was attempted on 2016 August 18, but it did not change the gain or resolution. A further attempt needs to be made to purify the gas in LAXPC20. The gain appears to be drifting at a rate of about 0.06 channels per day. For LAXPC10 the purification cycle on 2016 August 18 shifted the gain as expected, but the energy resolution did not improve. Nevertheless, the resolution of LAXPC10 appears to be stable over the past year. The

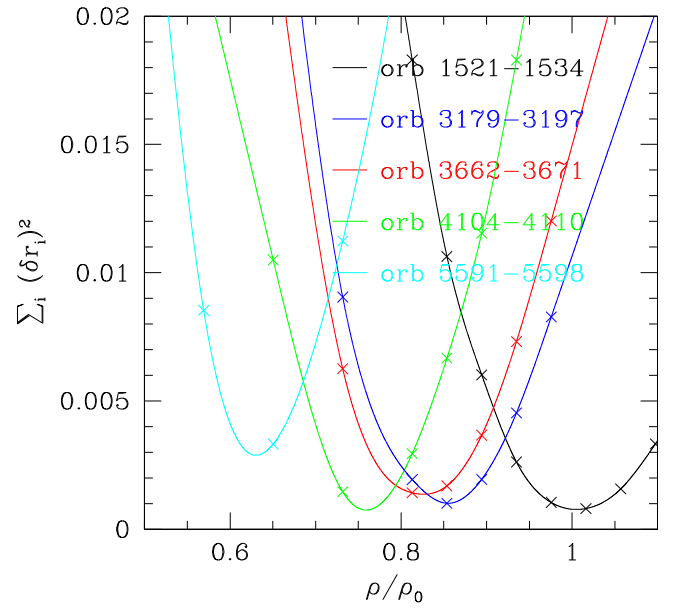


Figure 33. The function $F_x(\rho)$ as defined in Equation (6), from five different observations of Cyg X-1 as a function of gas density in LAXPC30.

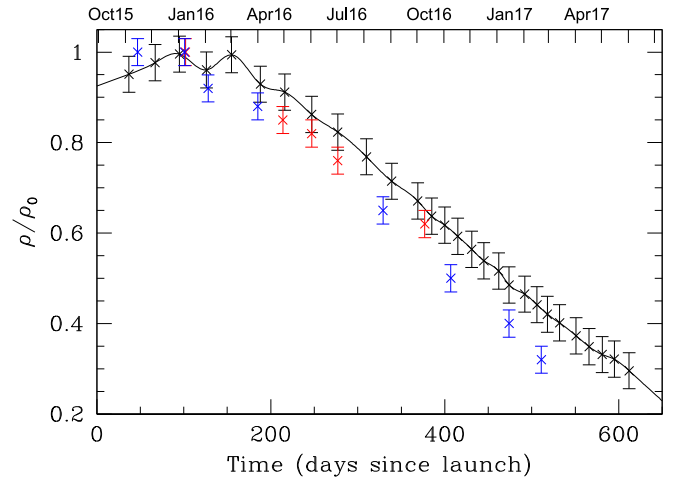


Figure 34. The density of gas in the LAXPC30 detector as a function of time using different techniques. The black points show the result using the onboard pressure gauge, which is normalized with respect to its maximum value; the red points are those using observations for Cyg X-1 (Figure 33) and the blue points are using observations for the Crab.

resolution of LAXPC30 is improving with time, presumably due to lower pressure.

A large part of the shift in gain can be adjusted by changing the linear term, the coefficient e_1 in Equation (3), but other coefficients may also be changing. Another measure of the change can be obtained by taking the ratio of the channels for the 60 keV and 30 keV peaks. The energy ratio of the two peaks is close to 2, and for a linear gain the ratio in channels should be 2, and any departure from this value could be due to the other two terms in Equation (3). Figure 36 shows the difference $2 - p_2/p_1$ where p_1 and p_2 are the positions of the 30 and 60 keV peaks. It can be seen that this ratio has been decreasing in magnitude for both LAXPC20 and LAXPC30, although it appears to have stabilized for LAXPC20 after 2016 May. Thus it is clear that the coefficients e_0 and e_2 are also changing with time. It is unlikely that all the observed variation can be accounted for by variation in e_0 because that will require

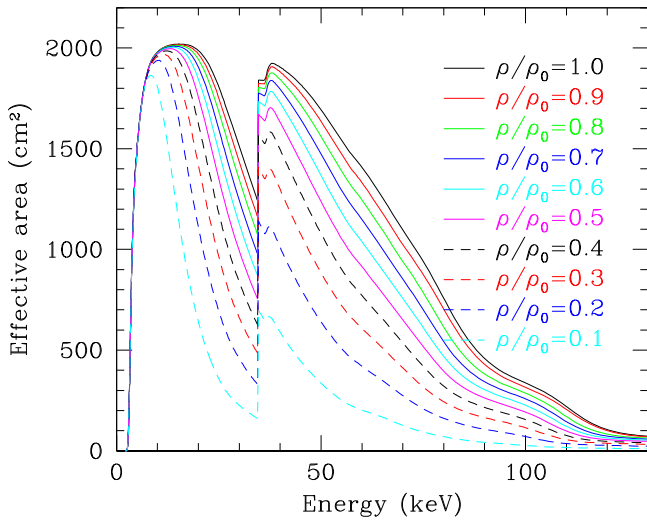


Figure 35. The effective area of LAXPC30 with different values of gas density. The values are in units of the original density.

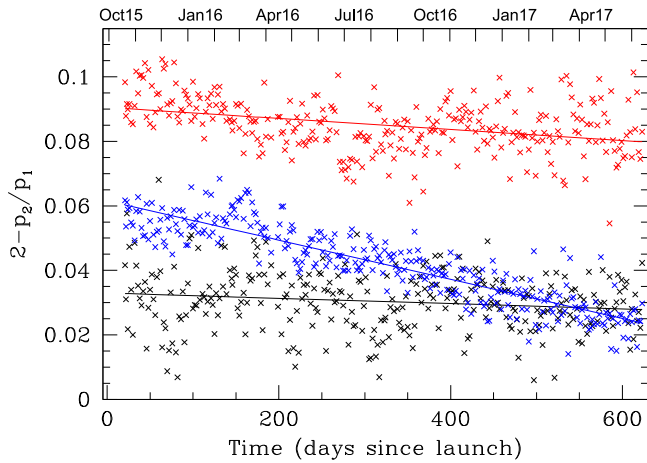


Figure 36. The difference $2 - p_2/p_1$, where p_1 and p_2 are the positions of the 30 and 60 keV peaks, for the three LAXPC detectors as a function of time. The black, red, and blue points respectively show the results for LAXPC10, LAXPC20, and LAXPC30. The time is measured in days from the launch of *AstroSat* on 2015 September 28. The solid line shows the linear fit to the points.

a large variation. Thus, it appears that e_2 is decreasing with time for these detectors.

To show the effect of a long-term variation in response, we have fitted the spectrum for the Crab during different observations using a response that is adjusted for the shift in gain and for a decrease in density in LAXPC30, and the results are shown in Figure 37. The fit for LAXPC20 and LAXPC30 during 2016 August is poor due to the shift in gain and decreasing density, respectively. There is also a general reduction in normalization for the fit during this observation, which is most likely due to a difference in pointing. For LAXPC30 the fitted power-law index, Γ , has also reduced. This is because the fit with lowest χ^2 with different densities has been selected. This probably underestimates the density and Γ . The use of a slightly higher density increases Γ , but also increases χ^2 .

Because of the leak, the efficiency of LAXPC30 is also changing as shown in Figure 35. As a result of this, the background count rate in LAXPC30 is decreasing with time.

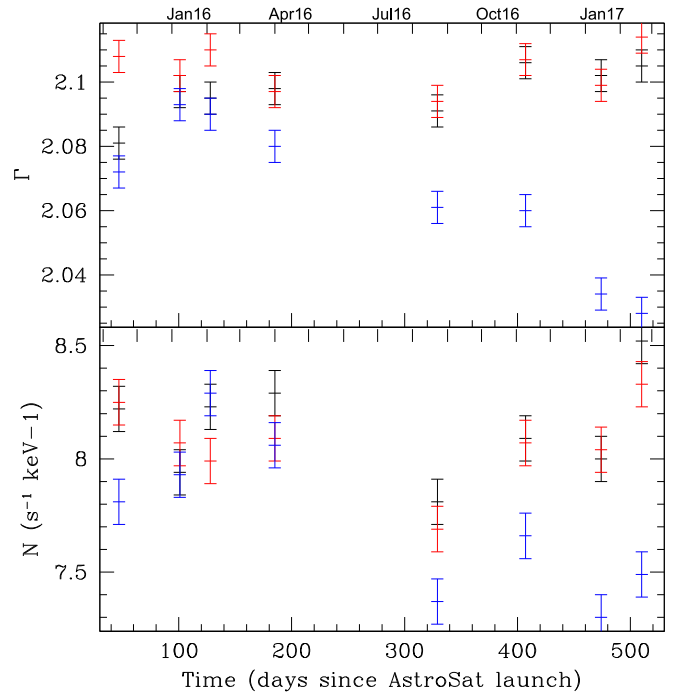


Figure 37. Fit of the Crab spectra observed at different times to a power-law model. The black, red, and blue points show the results for LAXPC10, LAXPC20, and LAXPC30 respectively.

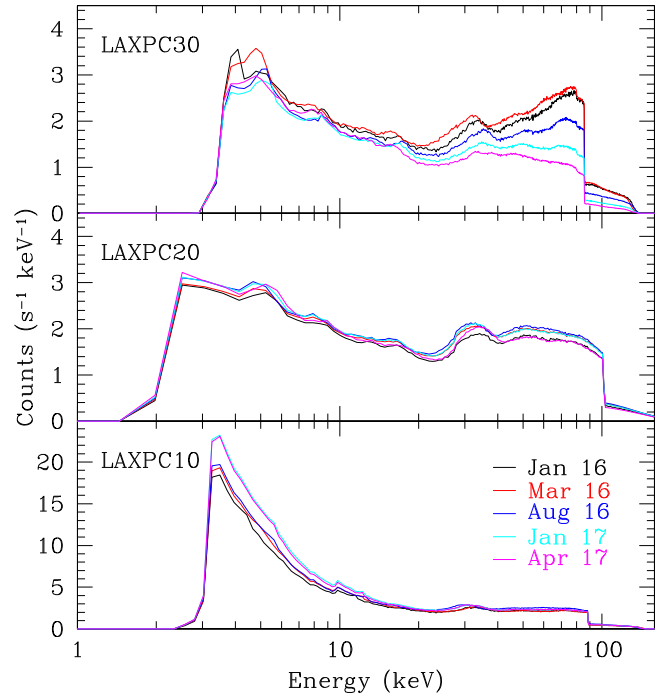


Figure 38. The background spectra for all LAXPC detectors taken at five different times.

Figure 38 compares the background observed during different times in the three detectors. It can be seen that for LAXPC30 the count rate is decreasing with time and the difference is greater at high energies. There is also some shift in the gain of LAXPC10 and LAXPC30, which also affected the background. The shift in the gain for all detectors can be seen from the position of the hump near 30 keV due to Xe K fluorescence X-rays. The background in LAXPC10 has increased

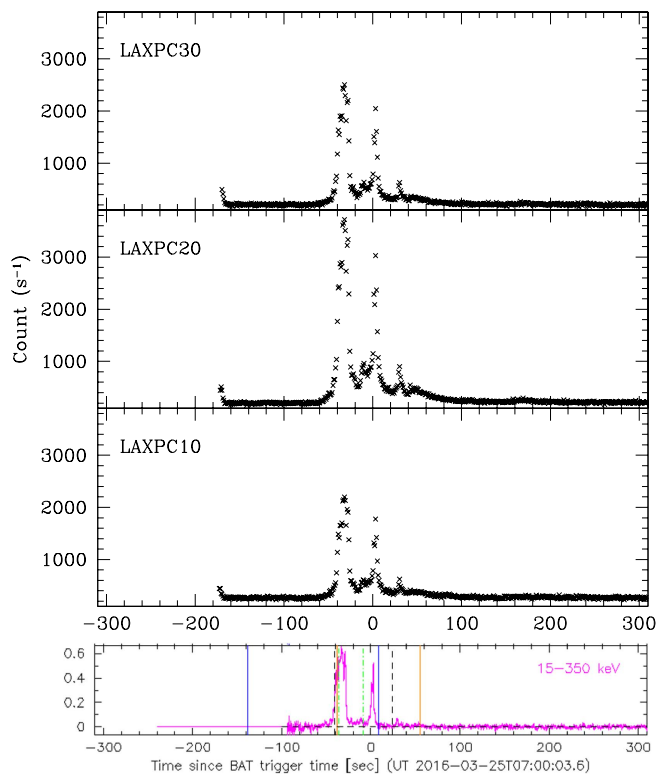


Figure 39. The light curve for GRB 160325A in the three LAXPC detectors. For comparison the lowest panel shows the light curve in *Swift*-BAT from http://gcn.gsfc.nasa.gov/notices_s/680436/BA/.

significantly during the last six months. The increase is seen mainly at low energies in all anodes that are adjacent to veto anode A10, which is disabled. The reason for this increase is not clear.

Apart from observing the scheduled sources, LAXPC has also detected a number of gamma-ray bursts (GRBs). The probability of occurrence of a GRB in the $1^\circ \times 1^\circ$ field of view of LAXPC is very low (about $1/40,000$) and hence almost all the registered GRBs are those that occur to the sides of the detectors. Gamma-rays from GRBs have hard spectra extending to several MeV and even beyond. Gamma-rays of hundreds of keV and MeV strike the side walls of the detector and produce secondary particles either in the walls of the detector housing or in the gas volume. Some of these may get detected as a genuine event. As pointed out in Section 4.4, there is about 1% probability that a high-energy photon coming from a random direction will register a valid event in the detector. An accurate time profile of the GRBs can be derived from time-tagged events. One of the events detected is shown in Figure 39. The detectors do not all record the same count rate, because depending on the direction of the burst with respect to the satellite, some detectors may be partially shielded by other material on the satellite. Bursts occurring during the SAA transit are obviously missed. Similarly, those bursts that are occulted by the Earth are also not seen. The timing of these GRBs matches that recorded in the LAXPC detectors. This gives us confidence in absolute timing accuracy at the level of 1 s. In principle, it is possible to obtain the spectrum of the events recorded in the LAXPC detectors during a GRB but the spectrum may not give much information because most of these events are from secondaries produced in the satellite. Since these photons are not coming from the top window, the

response matrix for the detector cannot be applied to study these events. Although LAXPC may not be useful for studying GRBs, the fact that it can detect these bursts should be kept in mind because some of these may be mistaken for bursts in the source being observed.

8. Summary

AstroSat has completed more than 620 days of operation and more than 9200 orbits so far. More than 600 pointings for about 250 distinct sources have been carried out. The response of the instrument is reasonably understood and has been used to produce scientific results (Yadav et al. 2016b; Misra et al. 2017; Verdhan Chauhan et al. 2017). The energy resolution of the detector at 30 and 60 keV is shown in Figure 31, which shows that the energy resolution of LAXPC10 is steady at $(15 \pm 2)\%$, while that in LAXPC20 is degrading slowly from about 12% just after launch to about 16% currently at 30 keV. On the other hand, the energy resolution of LAXPC30 has improved from about 11% just after launch to better than 10% currently. The effective area of the detectors is shown in Figure 19 and its normalization depends on the pointing direction. The uncertainties in normalization can be estimated from the results for the Crab shown in Figure 37, which shows a variation of $\pm 5\%$. The LAXPC10 detector has a higher background count because one of the veto anodes is not functioning, while LAXPC30 has developed a leak and hence its sensitivity is decreasing at high energies as shown in Figure 35. The gain of all detectors is shifting with time and is controlled in a reasonable range by adjusting the high voltage from time to time. This shift has to be accounted for in spectral analysis.

The background model has uncertainties of up to 5% because of variation between different regions or satellite environments. The relatively large background in the LAXPC detectors and its variation with time limits its ability to observe faint sources. The background uncertainty corresponds to about 10 counts per second, while the Crab yields about 3000 counts per second in each detector, which limits the study of faint sources. It may not be possible to study sources fainter than a few mcrab. Similarly, the variation in gain with time and the understanding of detector response limit the scope of spectral studies. At the same time, a large area, and consequently a higher count rate and event analysis mode data, allows detailed timing studies to be carried out. While interpreting the power spectrum the possibility of instrumental features around 8–11 Hz in all detectors and around 50 Hz in LAXPC20 should be considered.

We acknowledge the strong support from the Indian Space Research Organization (ISRO) in various aspects of instrument building, testing, software development, and mission operation during the payload verification phase. We acknowledge support from the TIFR central workshop during the design and testing of the payload. We thank Dipankar Bhattacharya for arranging simultaneous observations with *NuSTAR* to calibrate the LAXPC instrument. We thank Tomaso Belloni for pointing out the feature around 50 Hz in the power spectrum of LAXPC20.

References

- Agostinelli, S., Allison, J., Amako, K., et al. 2003, *NIMPR*, **A506**, 250
 Agrawal, P. C. 2006, *AdSpR*, **38**, 2989
 Agrawal, P. C., Yadav, J. S., Antia, H. M., et al. 2017, *JApA*, **38**, 30

- Antia, H. M. 2012, *Numerical Methods for Scientists and Engineers* (3rd ed.; New Delhi: Hindustan Book Agency)
- Dean, A. J., Lei, F., & Knight, P. J. 1991, *SSRv*, **57**, 109
- Dias, T. H. V. T., dos Santos, J. M. F., Rachinhas, P. J. B. M., et al. 1997, *JAP*, **82**, 2742
- Dias, T. H. V. T., Santos, F. P., Stauffer, A. D., & Conde, C. A. N. 1991, *NIMPR*, **A307**, 341
- Dias, T. H. V. T., Santos, F. P., Stauffer, A. D., & Conde, C. A. N. 1993, *PhRvA*, **48**, 2887
- Harrison, F. A., Craig, W. W., Christensen, F. E., et al. 2013, *ApJ*, **770**, 103
- Jahoda, K., Markwardt, C. B., Radeva, Y., et al. 2006, *ApJ*, **163**, 401
- Knoll, G. F. 2000, *Radiation Detection and Measurement* (3rd ed.; New York: Wiley)
- Mandrou, P., Vedrenne, G., & Niel, M. 1979, *ApJ*, **230**, 97
- Misra, R., Yadav, J. S., Chauhan, J. V., et al. 2017, *ApJ*, **835**, 195
- Rao, A. R., Agrawal, P. C., Manchanda, R. K., & Shah, M. R. 1987, *AdSpR*, **7**, 129
- Revnitsev, M., Gilfanov, M., Sunyaev, R., Jahoda, K., & Markwardt, C. 2003, *A&A*, **411**, 329
- Schonfelder, V., Graml, F., & Penningsfeld, F. P. 1980, *ApJ*, **240**, 350
- Singh, K. P., Tandon, S. N., Agrawal, P. C., et al. 2014, *Proc. SPIE*, **9144**, 91441S
- Verdhan Chauhan, J., Yadav, J. S., Misra, R., et al. 2017, *ApJ*, **841**, 41
- Yadav, J. S., Agrawal, P. C., Antia, H. M., et al. 2016, *Proc. SPIE*, **9905**, 99051D
- Yadav, J. S., Mishra, R., Chauhan, J. V., et al. 2016, *ApJ*, **833**, 27
- Yamaguchi, H., Badenes, C., Petre, R., et al. 2014, *ApJL*, **785**, L27
- Zhang, W., Jahoda, K., Swank, J. H., Morgan, E. H., & Giles, A. B. 1995, *ApJ*, **449**, 930